Chapter 6

Beyond the Boussinesq Approximation

The Boussinesq eddy-viscosity approximation assumes the principal axes of the Reynolds-stress tensor, τ_{ij}, are coincident with those of the mean strain-rate tensor, S_{ij}, at all points in a turbulent flow. This is the analog of Stokes' approximation for laminar flows. The coefficient of proportionality between τ_{ij} and S_{ij} is the eddy viscosity, μ_T. Unlike the molecular viscosity which is a property of the fluid, the eddy viscosity depends upon many details of the flow under consideration. It is affected by the shape and nature (e.g., roughness height) of any solid boundaries, freestream turbulence intensity, and, perhaps most significantly, flow history effects. Experimental evidence indicates that flow history effects on τ_{ij} often persist for long distances in a turbulent flow, thus casting doubt on the validity of a simple linear relationship between τ_{ij} and S_{ij}. In this chapter, we examine several flows for which the Boussinesq approximation yields a completely unsatisfactory description. We then examine some of the remedies that have been proposed to provide more accurate predictions for such flows. Although our excursion into the realm beyond the Boussinesq approximation is brief, we will see how useful the analytical tools developed in preceding chapters are for even the most complicated turbulence models.

6.1   Boussinesq-Approximation Deficiencies

While models based on the Boussinesq eddy-viscosity approximation provide excellent predictions for many flows of engineering interest, there are some applications for which predicted flow properties differ greatly from

corresponding measurements. Generally speaking, such models are inaccurate for flows with sudden changes in mean strain rate and for flows with what Bradshaw (1973a) refers to as **extra rates of strain**. It is unsurprising that flows with sudden changes in mean strain rate pose a problem. The Reynolds stresses adjust to such changes at a rate unrelated to mean flow processes and time scales, so that the Boussinesq approximation must fail. Similarly, when a flow experiences extra rates of strain caused by rapid dilatation, out of plane straining, or significant streamline curvature, all of which give rise to unequal normal Reynolds stresses, the approximation again becomes suspect. Some of the most noteworthy types of applications for which models based on the Boussinesq approximation fail are:

1. flows with sudden changes in mean strain rate;

2. flow over curved surfaces;

3. flow in ducts with secondary motions;

4. flow in rotating and stratified fluids;

5. three-dimensional flows;

6. flows with boundary-layer separation.

As an example of a flow with a sudden change in strain rate, consider the experiment of Tucker and Reynolds (1968). In this experiment, a nearly isotropic turbulent flow is subjected to uniform mean normal strain rate attending the following mean velocity field:

$$U = \text{constant}, \quad V = -ay, \quad W = az \qquad (6.1)$$

The coefficient a is the constant strain rate. The strain rate is maintained for a finite distance in the x direction in the experiment and then removed. The turbulence becomes anisotropic as a result of the uniform straining, and gradually approaches isotropy downstream of the point where the straining ceases. Wilcox and Rubesin (1980) have applied their k-ω^2 model to this flow to demonstrate the deficiency of the Boussinesq approximation for flows in which mean strain rate abruptly changes. Figure 6.1 compares the computed and measured distortion parameter, K, defined by

$$K \equiv \frac{\overline{v'^2} - \overline{w'^2}}{\overline{v'^2} + \overline{w'^2}} \qquad (6.2)$$

As shown, when the strain rate is suddenly removed at $x \approx 2.3$ m, the model predicts an instantaneous return to isotropy, i.e., all normal Reynolds
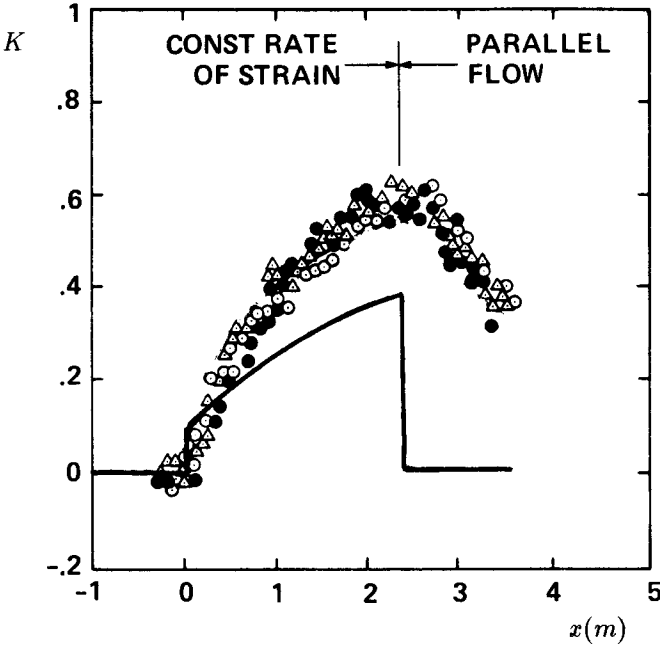
Figure 6.1: Computed and measured distortion parameter for the Tucker-Reynolds plane-strain flow; ——— k-ω^2 model; o • △ Tucker-Reynolds. [From Wilcox and Rubesin (1980).]

stresses become equal. By contrast, the turbulence approaches isotropy at a finite rate. Note also that the model predicts a discontinuous jump in K when the straining begins at $x = 0$ m. Interestingly, if the computation is extended downstream of $x = 2.3$ m without removing the strain rate, the model predicted asymptotic value of K matches the measured value at $x = 2.3$ m, but approaches this value at a slower than measured rate.

As an example of a flow with significant streamline curvature, consider flow over a curved surface. Meroney and Bradshaw (1975) find that for both convex and concave walls, when the radius of curvature, $\mathcal{R}$, is 100 times the local boundary-layer thickness, δ, skin friction differs from its corresponding plane-wall value by as much as 10%. By contrast, laminar skin friction changes by about 1% for $\delta/\mathcal{R} = .01$. Similar results have been obtained by Thomann (1968) for supersonic boundary layers; for constant-pressure flow over surfaces with $\delta/\mathcal{R} \sim .02$, heat transfer changes by nearly 20%. Clearly, many practical aerodynamic surfaces are sufficiently curved to produce significant curvature effects. For such flows, a reliable turbulence
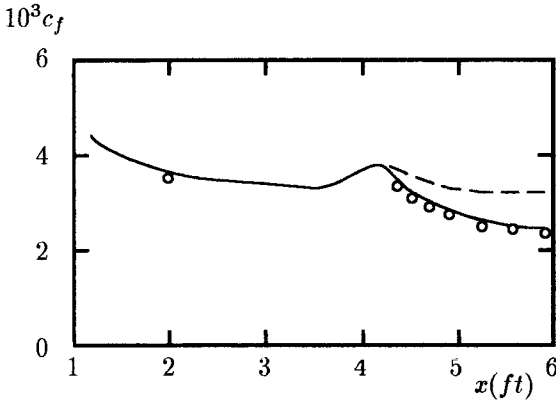
Figure 6.2: Computed and measured skin friction for flow over a convex surface with constant pressure; - - - k-ω model without curvature correction; —— k-ω model with curvature correction; o So and Mellor.

model must be capable of predicting effects of curvature on the turbulence.

Figure 6.2 compares computed and measured skin friction for flow over a convex wall. The flow, experimentally investigated by So and Mellor (1972), has nearly constant pressure. The wall is planar up to $x = 4.375$ ft and has $\delta/\mathcal{R} \sim .075$ beyond that location. As shown, computed skin friction is generally 30% to 40% higher than measured.

Wilcox and Chambers (1977) propose a curvature correction to the turbulence energy equation that provides an accurate prediction for flow over curved surfaces. Appealing to the classical stability arguments for flow over a curved wall advanced by von Kármán (1934), they postulate that the equation for k should more appropriately be thought of as the equation for $\overline{v'^2}$. Consequently, Wilcox and Chambers add a term originating from the centrifugal acceleration in the exact $\overline{v'^2}$ equation. For the Standard k-ω model, the boundary layer form of the equations for flow over a curved surface with radius of curvature, $\mathcal{R}$, are as follows.

$$U\frac{\partial U}{\partial x} + V\frac{\partial U}{\partial y} = -\frac{1}{\rho}\frac{dP}{dx} + \frac{\partial}{\partial y}\left[(\nu + \nu_T)\left(\frac{\partial U}{\partial y} - \frac{U}{\mathcal{R}}\right)\right], \quad \nu_T = \frac{k}{\omega} \quad (6.3)$$

$$U\frac{\partial k}{\partial x} + V\frac{\partial k}{\partial y} + \frac{9}{2}\nu_T\frac{U}{\mathcal{R}}\frac{\partial U}{\partial y} = \nu_T\left(\frac{\partial U}{\partial y} - \frac{U}{\mathcal{R}}\right)^2 - \beta^*\omega k + \frac{\partial}{\partial y}\left[(\nu + \sigma^*\nu_T)\frac{\partial k}{\partial y}\right]$$
$$(6.4)$$

The last term on the left-hand side of Equation (6.4) is the Wilcox-Chambers curvature-correction term. As shown in Figure 6.2, including the curvature term brings model predictions into much closer agreement with measurements. A perturbation analysis of Equations (6.3) to (6.5) for the log layer (see Problems) shows that the model predicts a modified law of the wall given by

$$\left[1 - \beta_R \frac{y}{\mathcal{R}}\right] \frac{U}{u_\tau} = \frac{1}{\kappa} \ell n \left(\frac{u_\tau y}{\nu}\right) + \text{constant} \tag{6.6}$$

with $\beta_R \approx 8.8$. This is very similar to the modified law of the wall deduced by Meroney and Bradshaw (1975), who conclude from correlation of measurements that $\beta_R \approx 12.0$.

Other curvature corrections have been proposed for two-equation models, and Lakshminarayana (1986) presents a comprehensive overview. Of

flow is compressible. Such models also fail to predict secondary motions that commonly occur in ducts, and in the absence of ad hoc corrections, fail to predict salient features of rotating and stratified flows. While these are more subtle and specialized applications, each failure underscores the fact that models based on the Boussinesq approximation are not universal. The following sections explore some of the proposals made to remove many of these deficiencies in a less ad hoc fashion.

6.2   Nonlinear Constitutive Relations

One approach to achieving a more appropriate description of the Reynolds-stress tensor without introducing any additional differential equations is to assume the Boussinesq approximation is simply the leading term in a series expansion of functionals. Proceeding with this premise, Lumley (1970) and Saffman (1976) show that for incompressible flow the expansion must proceed through second order according to

$$\tau_{ij} = -\frac{2}{3}\rho k \delta_{ij} + 2\mu_T S_{ij} - B\frac{\rho k}{\omega^2}S_{mn}S_{nm}\delta_{ij} - C\frac{\rho k}{\omega^2}S_{ik}S_{kj}$$
$$-D\frac{\rho k}{\omega^2}\left(S_{ik}\Omega_{kj} + S_{jk}\Omega_{ki}\right) - F\frac{\rho k}{\omega^2}\Omega_{mn}\Omega_{nm}\delta_{ij} - G\frac{\rho k}{\omega^2}\Omega_{ik}\Omega_{kj} \qquad (6.9)$$

where B, C, D, F and G are closure coefficients, and k/ω^2 may be equivalently written as k^3/ϵ^2. Also, S_{ij} and Ω_{ij} are the mean strain-rate and rotation tensors, viz.,

$$S_{ij} = \frac{1}{2}\left(\frac{\partial U_i}{\partial x_j} + \frac{\partial U_j}{\partial x_i}\right) \quad \text{and} \quad \Omega_{ij} = \frac{1}{2}\left(\frac{\partial U_i}{\partial x_j} - \frac{\partial U_j}{\partial x_i}\right) \qquad (6.10)$$

In order to guarantee that the trace of τ_{ij} is $-2\rho k$, we must have $B = -C/3$ and $F = -G/3$. Equation (6.9) can be simplified by requiring it to conform with certain fundamental experimental observations. In the experiment of Tucker and Reynolds (1968), for example, the normal Reynolds stresses are related approximately by

$$\tau_{xx} \approx \frac{1}{2}(\tau_{yy} + \tau_{zz}) \qquad (6.11)$$

Substituting Equations (6.1) and (6.11) into Equation (6.9) shows that necessarily $C = 0$. In addition, Ibbetson and Tritton (1975) show that homogeneous turbulence in rigid body rotation decays without developing anisotropy. This observation requires $G = 0$. Finally, if Equation (6.9) with $C = G = 0$ is applied to a classical shear layer where the only significant

velocity gradient is $\partial U/\partial y$, Equation (6.11) again applies with τ_{xx} and τ_{zz} interchanged, independent of the value of D. Thus, Saffman's general expansion simplifies to:

$$\tau_{ij} = -\frac{2}{3}\rho k \delta_{ij} + 2\mu_T S_{ij} - D\frac{\rho k}{\omega^2}\left(S_{ik}\Omega_{kj} + S_{jk}\Omega_{ki}\right) \qquad (6.12)$$

In analogy to this result, Wilcox and Rubesin (1980) propose the following simplified **nonlinear constitutive relation** for their k-ω^2 model.

$$\tau_{ij} = -\frac{2}{3}\rho k \delta_{ij} + 2\mu_T\left(S_{ij} - \frac{1}{3}\frac{\partial U_k}{\partial x_k}\delta_{ij}\right) + \frac{8}{9}\frac{\rho k(S_{ik}\Omega_{kj} + S_{jk}\Omega_{ki})}{(\beta^*\omega^2 + 2S_{mn}S_{nm})} \qquad (6.13)$$

The primary usefulness of this prescription for the Reynolds-stress tensor is in predicting the normal stresses. The coefficient 8/9 is selected to guarantee

$$\overline{u'^2} : \overline{v'^2} : \overline{w'^2} = 4 : 2 : 3 \qquad (6.14)$$

for the flat-plate boundary layer. Equation (6.14) is a good approximation throughout the log layer and much of the defect layer. The model faithfully predicts the ratio of the normal Reynolds stresses for boundary layers with adverse pressure gradient where the ratios are quite different from those given in Equation (6.14). Bardina, Ferziger and Reynolds (1983) have used an analog of this stress/strain-rate relationship in their Large Eddy Simulation studies. However, the model provides no improvement for flows over curved surfaces.

Speziale (1987b) proposes a nonlinear constitutive relation for the k-ϵ model as follows (for incompressible flow):

$$\tau_{ij} = -\frac{2}{3}\rho k \delta_{ij} + 2\mu_T S_{ij} + 4C_D C_\mu^2 \frac{\rho k^3}{\epsilon^2}\left(S_{ik}S_{kj} - \frac{1}{3}S_{mn}S_{nm}\delta_{ij}\right)$$
$$+ 4C_E C_\mu^2 \frac{\rho k^3}{\epsilon^2}\left(\overset{\circ}{S}_{ij} - \frac{1}{3}\overset{\circ}{S}_{mm}\delta_{ij}\right) \qquad (6.15)$$

where $\overset{\circ}{S}_{ij}$ is the frame-indifferent Oldroyd derivative of S_{ij} defined by

$$\overset{\circ}{S}_{ij} = \frac{\partial S_{ij}}{\partial t} + U_k\frac{\partial S_{ij}}{\partial x_k} - \frac{\partial U_i}{\partial x_k}S_{kj} - \frac{\partial U_j}{\partial x_k}S_{ki} \qquad (6.16)$$

The closure coefficients C_D and C_E are given by

$$C_D = C_E = 1.68 \qquad (6.17)$$

In addition to its elegance and simplicity, this model satisfies three key criteria that assure consistency with properties of the exact Navier-Stokes

equation. **First**, like the Saffman and Wilcox-Rubesin models, it satisfies general coordinate and dimensional invariance. **Second**, it satisfies a limited form of the Lumley (1978) realizability constraints (i.e., positiveness of $k \equiv -\frac{1}{2}\tau_{ii}$). **Third**, it satisfies material frame indifference in the limit of two-dimensional turbulence. The latter consideration leads to introduction of the Oldroyd derivative of S_{ij}.

The appearance of the rate of change of S_{ij} in the constitutive relation is appropriate for a viscoelastic-like medium. While, to some degree, the Speziale constitutive relation includes rate effects, it still fails to describe the gradual adjustment of the Reynolds stresses following a sudden change in strain rate. For example, consider the Tucker-Reynolds flow discussed above. The Oldroyd derivative of S_{ij} is given by

$$\overset{\circ}{S}_{yy} = \overset{\circ}{S}_{zz} = -2a^2; \quad \text{all other} \quad \overset{\circ}{S}_{ij} = 0 \qquad (6.18)$$

Clearly, when the strain rate is abruptly removed, the Speziale model predicts that the normal Reynolds stresses instantaneously return to isotropy. Hence, the model is no more accurate than the Wilcox-Rubesin model for such flows.

For flow over a curved surface, the contribution of the nonlinear terms in the Speziale model to the shear stress is negligible. Consequently, this model, like the Wilcox-Rubesin model, offers no improvement over the Boussinesq approximation for curved-wall flows.

While the model fails to improve model predictions for flows with sudden changes in strain rate and flows with curved streamlines, it does make a dramatic difference for flow through a rectangular duct [see Figure 6.3(a)]. For such a flow, the difference between τ_{zz} and τ_{yy} according to Speziale's relation is, to leading order,

$$\tau_{zz} - \tau_{yy} = C_D C_\mu^2 \frac{\rho k^3}{\epsilon^2} \left[\left(\frac{\partial U}{\partial z} \right)^2 - \left(\frac{\partial U}{\partial y} \right)^2 \right] \qquad (6.19)$$

while, to the same order, the shear stresses are

$$\tau_{xy} = \mu_T \frac{\partial U}{\partial y}, \quad \tau_{xz} = \mu_T \frac{\partial U}{\partial z}, \quad \tau_{yz} = C_D C_\mu^2 \frac{\rho k^3}{\epsilon^2} \frac{\partial U}{\partial y} \frac{\partial U}{\partial z} \qquad (6.20)$$

Having a difference between τ_{zz} and τ_{yy} is critical in accurately simulating secondary motions. Using his model, Speziale (1987b) has computed flow through a rectangular duct. Figure 6.3(b) shows computed secondary flow streamlines, which clearly illustrates that there is an eight-vortex secondary flow structure as seen in experiments. Using the Boussinesq approximation, no secondary flow develops, so that the Speziale model obviously

(a) Flow geometry   (b) Secondary flow streamlines
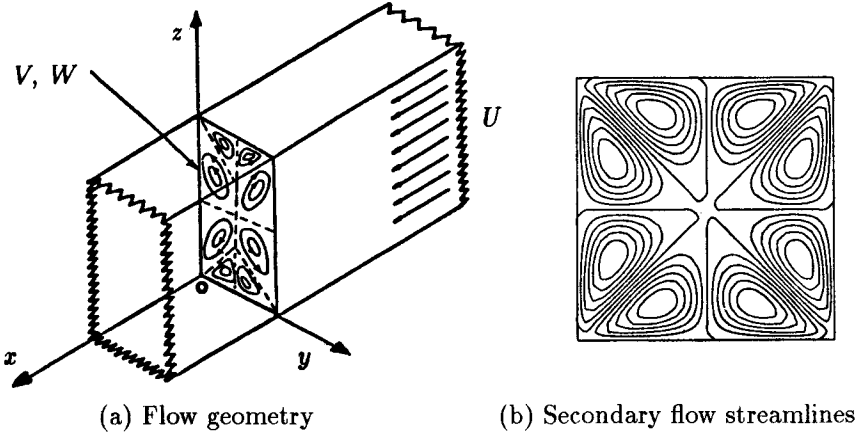
Figure 6.3: Fully developed turbulent flow in a rectangular duct. [From Speziale (1991) — Published with permission of author.]

does a better job of capturing this missing feature. Although Speziale presents no comparison of computed and measured results, the net effect of the nonlinear terms is very dramatic.

Speziale's nonlinear constitutive relation also improves k-ϵ model predictions for the backward-facing step. Focusing on the experiment of Kim, Kline and Johnston (1980), Thangam and Speziale (1992) have shown that using the nonlinear model with a low-Reynolds-number k-ϵ model increases predicted reattachment length for this flow from 6.3 step heights to 6.9 step heights. The measured length is 7.0 step heights.

Rodi (1976) deduces a nonlinear constitutive equation by working with a model for the full Reynolds-stress equation [Equation (2.34)]. Rodi begins by approximating the difference between convective and turbulent transport terms for incompressible flow as:

$$\frac{\partial \tau_{ij}}{\partial t} + U_k \frac{\partial \tau_{ij}}{\partial x_k} - \frac{\partial}{\partial x_k}\left[\nu \frac{\partial \tau_{ij}}{\partial x_k} + C_{ijk}\right]$$
$$\approx \frac{\tau_{ij}}{k}\left\{\frac{\partial k}{\partial t} + U_k \frac{\partial k}{\partial x_k} - \frac{\partial}{\partial x_k}\left[\nu \frac{\partial k}{\partial x_k} + \frac{C_{jjk}}{2\rho}\right]\right\} \quad (6.21)$$

This approximation yields a nonlinear algebraic equation that can be used to determine the Reynolds-stress tensor, viz.,

$$\frac{\tau_{ij}}{\rho k}\left\{\tau_{mn}\frac{\partial U_m}{\partial x_n} - \rho\epsilon\right\} = -\tau_{ik}\frac{\partial U_j}{\partial x_k} - \tau_{jk}\frac{\partial U_i}{\partial x_k} + \epsilon_{ij} - \Pi_{ij} \quad (6.22)$$

With suitable closure approximations for the dissipation tensor, ϵ_{ij}, and the pressure-strain correlation tensor, Π_{ij}, Equation (6.22) defines a nonlinear constitutive relation. More precisely, Gatski and Speziale (1992) regard such models as strain-dependent generalizations of nonlinear constitutive relations. That is, these models can be written in a form similar to Saffman's expansion [Equation (6.9)]. The various closure coefficients then become functions of certain Reynolds-stress tensor invariants. The complexity of the constitutive relation depends on the closure approximations, and alternative approximations have been tried by many researchers [see Lakshminarayana (1986)]. A model derived in this manner is known as an **Algebraic Stress Model** or, in abbreviated form, as an **ASM**.

When an ASM is used for a flow with zero mean strain rate, Equation (6.22) simplifies to

$$\tau_{ij} = \frac{k}{\epsilon}\left(\Pi_{ij} - \epsilon_{ij}\right) \tag{6.23}$$

As we will discuss in Subsection 6.3.1, in the limit of vanishing mean strain rate, the most common closure approximations for ϵ_{ij} and Π_{ij} simplify to

$$\Pi_{ij} \rightarrow C_1 \frac{\epsilon}{k}\left(\tau_{ij} + \frac{2}{3}\rho k \delta_{ij}\right) \quad \text{and} \quad \epsilon_{ij} \rightarrow \frac{2}{3}\rho\epsilon\delta_{ij} \tag{6.24}$$

where C_1 is a closure coefficient. Hence, when the mean strain rate vanishes, the algebraic stress model simplifies to

$$\tau_{ij} = -\frac{2}{3}\rho k \delta_{ij} \tag{6.25}$$

This shows that the ASM predicts an instantaneous return to isotropy in the Tucker-Reynolds flow discussed above. Hence, like the Wilcox-Rubesin and Speziale nonlinear constitutive relations, the ASM fails to properly account for sudden changes in the mean strain rate. The ASM does provide significant improvement for flows with streamline curvature however. So and Mellor (1978), for example, show that excellent agreement between computed and measured flow properties is possible using an ASM with the k-ϵ model for boundary layers on curved surfaces. The model predicts most qualitative features and provides fair quantitative agreement for flows with secondary motions as shown, for example, by Demuren (1991).

In summary, the primary advantage of nonlinear constitutive relations appears to be in predicting the anisotropy of the normal Reynolds stresses. The most important application for which this is of interest is for flow in ducts with secondary motions. In the case of algebraic stress models, greatly improved predictions can be obtained for flows with nontrivial streamline curvature. It is doubtful that the nonlinear stress models discussed in this

section yield any significant improvement for separating and reattaching flows. While the k-ϵ model's predicted reattachment length is closer to the measured length when the nonlinear model is used, it is not clear that a better description of the physics of this flow has been provided. The excellent solutions obtained with the Standard k-ω model [see Section 4.10] strongly suggest that the k-ϵ model's inaccuracy for such flows has nothing to do with the basic eddy-viscosity assumption. While the improvements attending use of a nonlinear constitutive relation with two-equation models are nontrivial, the models still retain many of their deficiencies.

6.3   Second-Order Closure Models

Although it poses a more formidable task with regard to establishing suitable closure approximations, there are potential gains in universality that can be realized by devising a second-order closure model. As we will see, such models naturally include effects of streamline curvature, sudden changes in strain rate, secondary motions, etc. We will also see that there is a significant price to be paid in complexity and computational difficulty for these gains.

Virtually all researchers use the same starting point for developing such a model, viz., the exact differential equation describing the behavior of the Reynolds-stress tensor, $\tau_{ij} \equiv -\rho\overline{u_i' u_j'}$. As shown in Chapter 2, the incompressible form of the exact equation is

$$\frac{\partial \tau_{ij}}{\partial t} + U_k \frac{\partial \tau_{ij}}{\partial x_k} = -\tau_{ik}\frac{\partial U_j}{\partial x_k} - \tau_{jk}\frac{\partial U_i}{\partial x_k} + \epsilon_{ij} - \Pi_{ij} + \frac{\partial}{\partial x_k}\left[\nu \frac{\partial \tau_{ij}}{\partial x_k} + C_{ijk} \right] \quad (6.26)$$

where

$$\Pi_{ij} = \overline{p'\left(\frac{\partial u_i'}{\partial x_j} + \frac{\partial u_j'}{\partial x_i} \right)} \quad (6.27)$$

$$\epsilon_{ij} = 2\mu\overline{\frac{\partial u_i'}{\partial x_k}\frac{\partial u_j'}{\partial x_k}} \quad (6.28)$$

and

$$C_{ijk} = \rho\overline{u_i' u_j' u_k'} + \overline{p'u_i'}\delta_{jk} + \overline{p'u_j'}\delta_{ik} \quad (6.29)$$

Inspection of Equation (6.26) shows why we can expect a second-order closure model to correct some of the Boussinesq approximation's shortcomings. **First**, since the equation automatically accounts for the convection and diffusion of τ_{ij}, a second-order closure model will include effects of flow history. The presence of dissipation and turbulent-transport terms indicates the presence of time scales unrelated to mean-flow time scales, so history

effects should be more realistically represented than with a two-equation model. **Second**, Equation (6.26) contains convection, production and (optionally) body-force terms that respond automatically to effects such as streamline curvature, system rotation and stratification, at least qualitatively. Thus, there is potential for naturally representing such effects with a well-formulated second-order closure model. **Third**, Equation (6.26) gives no a priori reason for the normal stresses to be equal even when the mean strain rate vanishes. Rather, their values will depend upon initial conditions and other flow processes, so that the model should behave properly for flows with sudden changes in strain rate.

Rotta (1951) was the first to accomplish closure of the Reynolds-stress equation, although he did not carry out numerical computations. Many researchers have made important contributions since the pioneering efforts of Rotta. Two of the most important conceptual contributions have been made by Donaldson and Lumley. Donaldson [c.f. Donaldson and Rosenbaum (1968)] was the first to advocate the concept of **invariant modeling**, i.e., establishing closure approximations that rigorously satisfy coordinate invariance. Lumley (1978) has developed a systematic procedure for representing closure approximations that guarantees **realizability**, i.e., that all physically positive-definite turbulence properties be computationally positive definite and that all computed correlation coefficients lie between ± 1. The next subsection discusses these, and other, concepts and their impact on closure approximations.

6.3.1   Closure Approximations

To close Equation (6.26), we must model the dissipation tensor, ϵ_{ij}, the turbulent-transport tensor, C_{ijk}, and the pressure-strain correlation tensor, Π_{ij}. Because each of these terms is a tensor, the approximations required for closure can assume much more elaborate forms compared to approximations used for the simpler scalar and vector terms in the k equation. In this subsection, we will discuss some of the most commonly used closure approximations.

Dissipation: Because dissipation occurs at the smallest scales, most modelers use the Kolmogorov (1941) hypothesis of local isotropy, which implies

$$\epsilon_{ij} = \frac{2}{3}\rho\epsilon\delta_{ij} \qquad (6.30)$$

where

$$\epsilon = \nu\overline{\frac{\partial u_i'}{\partial x_k}\frac{\partial u_i'}{\partial x_k}} \qquad (6.31)$$

The scalar quantity ϵ is exactly the dissipation rate appearing in the turbulence kinetic energy equation. Contracting Equation (6.26) shows that this must be the case. As with simpler models, we must establish a procedure for determining ϵ. In most of his work, for example, Donaldson has specified ϵ algebraically, similar to what is done with a one-equation model. Most researchers use the ϵ equation as formulated for the k-ϵ model. Wilcox and Rubesin (1980) and Wilcox (1988b) compute ϵ by using an equation for the specific dissipation rate.

Since the dissipation is in reality anisotropic, particularly close to solid boundaries, some efforts have been made to model this effect. Generalizing a low-Reynolds-number proposal of Rotta (1951), Hanjalić and Launder (1976), for example, postulate that

$$\epsilon_{ij} = \frac{2}{3}\rho\epsilon\delta_{ij} + 2f_s\rho\epsilon b_{ij} \qquad (6.32)$$

where b_{ij} is the dimensionless **Reynolds-stress anisotropy tensor**, viz.,

$$b_{ij} = -\left(\frac{\tau_{ij} + \frac{2}{3}\rho k\delta_{ij}}{2\rho k}\right) \qquad (6.33)$$

and f_s is a low-Reynolds-number damping function, which they choose empirically to vary with turbulence Reynolds number, $Re_T \equiv k^2/(\epsilon\nu)$, according to

$$f_s = \left(1 + \frac{1}{10}Re_T\right)^{-1} \qquad (6.34)$$

Turbulent Transport: As with the turbulence energy equation, pressure fluctuations, as well as triple products of velocity fluctuations, appear in the tensor C_{ijk}. Definitive experimental data are unavailable to provide any guidance for modeling the pressure-correlation terms, and they are effectively ignored. The most common approach used in modeling C_{ijk} is to assume a gradient transport process. Donaldson (1972), for example, argues that the simplest tensor of rank three that can be obtained from the second-order correlation τ_{ij} is $\partial\tau_{ik}/\partial x_j$. Since C_{ijk} is symmetric in all three of its indices, he concludes that

$$C_{ijk} \sim \frac{\partial\tau_{jk}}{\partial x_i} + \frac{\partial\tau_{ik}}{\partial x_j} + \frac{\partial\tau_{ij}}{\partial x_k} \qquad (6.35)$$

This tensor has the proper symmetry, but is not dimensionally correct. We require a factor whose dimensions are length^2/time — a gradient diffusivity — and the ratio of k^2/ϵ has been employed by Mellor and Herring (1973)

and Launder, Reece and Rodi (1975). Using the notation of Launder et al., the final form of the closure approximation is

$$C_{ijk} = \frac{2}{3} C_s \frac{k^2}{\epsilon} \left[\frac{\partial \tau_{jk}}{\partial x_i} + \frac{\partial \tau_{ik}}{\partial x_j} + \frac{\partial \tau_{ij}}{\partial x_k} \right] \tag{6.36}$$

where $C_s \approx 0.11$ is a scalar closure coefficient.

Launder, Reece and Rodi also postulate a more general form based on analysis of the transport equation for C_{ijk}. Through a series of heuristic arguments, they infer the following alternative closure approximation:

$$C_{ijk} = -C_s' \frac{k}{\rho \epsilon} \left[\tau_{im} \frac{\partial \tau_{jk}}{\partial x_m} + \tau_{jm} \frac{\partial \tau_{ik}}{\partial x_m} + \tau_{km} \frac{\partial \tau_{ij}}{\partial x_m} \right] \tag{6.37}$$

where $C_s' \approx 0.25$ is also a scalar closure coefficient.

Pressure-Strain Correlation: The tensor Π_{ij}, which is often referred to as the **pressure-strain redistribution** term, has received the greatest amount of attention from turbulence modelers. The reason for this interest is twofold. First, being of the same order as production, the term plays a critical role in most flows of engineering interest. Second, because it involves essentially unmeasurable correlations, a great degree of cleverness and ingenuity is required to establish a rational closure approximation.

To determine pressure fluctuations in an incompressible flow we must, in principle, solve the following Poisson equation for p'.

$$\frac{1}{\rho} \nabla^2 p' = -2 \frac{\partial U_i}{\partial x_j} \frac{\partial u_j'}{\partial x_i} - \frac{\partial^2}{\partial x_i \partial x_j} \left(u_i' u_j' - \overline{u_i' u_j'} \right) \tag{6.38}$$

This equation follows from taking the divergence of the Navier-Stokes equation and subtracting the time-averaged equation from the instantaneous equation. The classical approach to solving this equation is to write p' as the sum of two contributions, viz.,

$$p' = p'_{slow} + p'_{rapid} \tag{6.39}$$

By construction, the **slow** and **rapid** pressure fluctuations satisfy the following equations.

$$\frac{1}{\rho} \nabla^2 p'_{slow} = -\frac{\partial^2}{\partial x_i \partial x_j} \left(u_i' u_j' - \overline{u_i' u_j'} \right) \tag{6.40}$$

$$\frac{1}{\rho} \nabla^2 p'_{rapid} = -2 \frac{\partial U_i}{\partial x_j} \frac{\partial u_j'}{\partial x_i} \tag{6.41}$$

The general notion implied by the nomenclature is changes in the mean strain rate contribute most rapidly to p'_{rapid} because the mean velocity gradient appears explicitly in Equation (6.41). By contrast, such effects are implicitly represented in Equation (6.40). The terminology **slow** and **rapid** should not be taken too literally, however, since the mean strain rate does not necessarily change more rapidly than $u'_i u'_j$.

For homogeneous turbulence, these equations can be solved in terms of appropriate Green's functions, and the resulting form of Π_{ij} is

$$\Pi_{ij} = A_{ij} + M_{ijkl} \frac{\partial U_k}{\partial x_l} \tag{6.42}$$

where A_{ij} is the **slow pressure strain** and the tensor $M_{ijkl}\partial U_k/\partial x_l$ is the **rapid pressure strain**. The tensors A_{ij} and M_{ijkl} are given by the following.

$$A_{ij} = \frac{1}{4\pi} \iiint_V \overline{\left(\frac{\partial u'_i}{\partial x_j} + \frac{\partial u'_j}{\partial x_i} \right) \frac{\partial^2 (u'_k u'_l)}{\partial y_k \partial y_l}} \frac{d^3 y}{|\mathbf{x} - \mathbf{y}|} \tag{6.43}$$

$$M_{ijkl} = \frac{1}{2\pi} \iiint_V \overline{\left(\frac{\partial u'_i}{\partial x_j} + \frac{\partial u'_j}{\partial x_i} \right) \frac{\partial u'_l}{\partial y_k}} \frac{d^3 y}{|\mathbf{x} - \mathbf{y}|} \tag{6.44}$$

The integration range for Equations (6.43) and (6.44) is the entire flowfield. Additionally, for inhomogeneous turbulence, the second term in Equation (6.42) becomes an integral with the mean velocity gradient inside the integrand. This emphasizes a shortcoming of single-point closure schemes that has not been as obvious in any of the closure approximations we have discussed thus far. That is, we are postulating that we can accomplish closure based on correlations of fluctuating quantities at the same physical location. The pressure-strain correlation very clearly is not a localized process, but rather, involves contributions from every point in the flow. This would suggest that two-point correlations, i.e., products of fluctuating properties at two separate physical locations, are more appropriate. Nevertheless, we expect contributions from more than one or two large eddy sizes away to be negligible, and this would effectively define what is usually referred to as the **locally homogeneous approximation**. Virtually all modelers assume that turbulent flows behave as though they are locally homogeneous, and use Equation (6.42).

The forms of the tensors A_{ij} and M_{ijkl} must adhere to a variety of constraints resulting from the symmetry of indices, mass conservation and other kinematic constraints. We know, for example, that the trace of Π_{ij} must vanish and this is true for the slow and rapid parts individually. Rotta

(1951) postulates that the **slow pressure-strain** term, often referred to as the **return-to-isotropy** term, is given by

$$A_{ij} = C_1 \frac{\epsilon}{k} \left(\tau_{ij} + \frac{2}{3} \rho k \delta_{ij} \right) \qquad (6.45)$$

where C_1 is a closure coefficient whose value can be inferred from measurements [Uberoi (1956)] to lie in the range

$$1.4 < C_1 < 1.8 \qquad (6.46)$$

Turning now to the **rapid pressure strain**, early research efforts of Donaldson [Donaldson and Rosenbaum (1968)], Daly and Harlow (1970), and Lumley (1972) assumed that the rapid pressure strain is negligible compared to the slow pressure strain. However, Crow (1968) and Reynolds (1970) provide simple examples of turbulent flows for which the effect of the rapid pressure strain far outweighs the slow pressure strain.

Launder, Reece and Rodi (1975) have devised a particularly elegant closure approximation based almost entirely on kinematical considerations. Building upon preliminary analysis of Rotta (1951), they write M_{ijkl} in terms of a tensor a_{ijkl} as follows.

$$M_{ijkl} = a_{ijkl} + a_{jikl} \qquad (6.47)$$

This relation is strictly valid only for homogeneous turbulence. Rotta demonstrates that the tensor a_{ijkl} must satisfy the following constraints:

$$a_{ijkl} = a_{ljki} = a_{lkji} \qquad (6.48)$$

and

$$a_{iikl} = 0, \qquad a_{ijjl} = -2\tau_{il} \qquad (6.49)$$

Launder et al. propose that the fourth-rank tensor a_{ijkl} can be expressed as a linear function of the Reynolds-stress tensor. The most general tensor, linear in τ_{ij}, satisfying the symmetry constraints of Equation (6.48) is

$$a_{ijkl} = -\alpha \delta_{kj} \tau_{li} - \beta(\delta_{lk} \tau_{ij} + \delta_{lj} \tau_{ik} + \delta_{ik} \tau_{lj} + \delta_{ij} \tau_{lk})$$
$$-C_2 \delta_{li} \tau_{kj} + [\eta \delta_{li} \delta_{kj} + \upsilon(\delta_{lk} \delta_{ij} + \delta_{lj} \delta_{ik})]\rho k \qquad (6.50)$$

where α, β, C_2, η and υ are closure coefficients. Invoking the conditions of Equation (6.49), all of the coefficients can be expressed in terms of C_2, viz.,

$$\alpha = \frac{4C_2 + 10}{11}, \quad \beta = -\frac{3C_2 + 2}{11}, \quad \eta = -\frac{50C_2 + 4}{55}, \quad \upsilon = \frac{20C_2 + 6}{55} \qquad (6.51)$$

Finally, combining Equations (6.47) through (6.51), we arrive at the well-known LRR model for the rapid pressure strain.

LRR Rapid Pressure-Strain Model:

$$M_{ijkl}\frac{\partial U_k}{\partial x_l} = -\hat{\alpha}\left(P_{ij} - \frac{1}{3}P_{kk}\delta_{ij}\right) - \hat{\beta}\left(D_{ij} - \frac{1}{3}D_{kk}\delta_{ij}\right) - \hat{\gamma}\rho k S_{ij} \quad (6.52)$$

$$P_{ij} = \tau_{im}\frac{\partial U_j}{\partial x_m} + \tau_{jm}\frac{\partial U_i}{\partial x_m} \quad \text{and} \quad D_{ij} = \tau_{im}\frac{\partial U_m}{\partial x_j} + \tau_{jm}\frac{\partial U_m}{\partial x_i} \quad (6.53)$$

$$\hat{\alpha} = \frac{8 + C_2}{11}, \quad \hat{\beta} = \frac{8C_2 - 2}{11}, \quad \hat{\gamma} = \frac{60C_2 - 4}{55}, \quad 0.4 < C_2 < 0.6 \quad (6.54)$$

Note that for compressible flows, the mean strain-rate tensor, S_{ij}, is usually replaced by $S_{ij} - \frac{1}{3}S_{kk}\delta_{ij}$ in Equation (6.52).

One of the most remarkable features of this closure approximation is the presence of just one undetermined closure coefficient, namely, C_2. The value of C_2 has been established by comparison of model predictions with measured properties of homogeneous turbulent flows. Launder, Reece and Rodi (1975) suggested using $C_2 = 0.40$. Morris (1984) revised its value upward to $C_2 = 0.50$, while Launder (1992) currently recommends $C_2 = 0.60$. Section 6.4 discusses the kind of flows used to calibrate this model.

Bradshaw (1973b) has shown that there is an additional contribution to Equations (6.43) and (6.44) that has a nontrivial effect close to a solid boundary. It is attributed to a surface integral that appears in the Green's function for Equation (6.38). This has come to be known as the **pressure-echo effect** or **wall-reflection effect**. Launder, Reece and Rodi (1975) propose a near-wall correction to their model for Π_{ij} that explicitly involves distance from the surface. Gibson and Launder (1978) and Craft and Launder (1992) propose alternative models to account for the pressure-echo effect. For example, the LRR wall-reflection term, $\Pi_{ij}^{(w)}$, is

$$\Pi_{ij}^{(w)} = \left[0.125\frac{\epsilon}{k}(\tau_{ij} + \frac{2}{3}\rho k \delta_{ij}) - 0.015(P_{ij} - D_{ij})\right]\frac{k^{3/2}}{\epsilon n} \quad (6.55)$$

where n is distance normal to the surface.

More recent efforts at devising a suitable closure approximation for Π_{ij} have focused on developing a nonlinear expansion in terms of the anisotropy tensor, b_{ij}, defined in Equation (6.33). Lumley (1978) has systematically developed a general representation for Π_{ij} based on Equations (6.38) through (6.44). In addition to insisting upon coordinate invariance and other required symmetries, Lumley insists upon **realizability**. As noted earlier, this means that all quantities known to be strictly positive must be

guaranteed to be positive by the closure model. Additionally, all computed correlation coefficients must lie between ± 1. This limits the possible form of the functional expansion for Π_{ij}. Lumley argues that the most general form of the complete tensor Π_{ij} for incompressible flow is as follows.

Lumley Pressure-Strain Model:

$$\Pi_{ij} = a_0 \rho \epsilon b_{ij} + a_1 \rho \epsilon \left(b_{ik} b_{jk} - \frac{1}{3} II \delta_{ij} \right) + a_2 \rho k S_{ij}$$

$$+ \rho k \left(a_3 b_{kl} S_{lk} + a_4 b_{kl} b_{lm} S_{mk} \right) b_{ij}$$

$$+ \rho k \left(a_5 b_{kl} S_{lk} + a_6 b_{kl} b_{lm} S_{mk} \right) \left(b_{ik} b_{kj} - \frac{1}{3} II \delta_{ij} \right)$$

$$+ a_7 \rho k \left(b_{ik} S_{jk} + b_{jk} S_{ik} - \frac{2}{3} b_{kl} S_{lk} \delta_{ij} \right)$$

$$+ a_8 \rho k \left(b_{ik} b_{kl} S_{jl} + b_{jk} b_{kl} S_{il} - \frac{2}{3} b_{kl} b_{lm} S_{mk} \delta_{ij} \right)$$

$$+ a_9 \rho k \left(b_{ik} \Omega_{jk} + b_{jk} \Omega_{ik} \right) + a_{10} \rho k \left(b_{ik} b_{kl} \Omega_{jl} + b_{jk} b_{kl} \Omega_{il} \right) \qquad (6.56)$$

The eleven closure coefficients are assumed to be functions of the **tensor invariants** II and III, i.e.,

$$a_i = a_i(II, III), \qquad II = b_{ij} b_{ij}, \qquad III = b_{ik} b_{kl} b_{li} \qquad (6.57)$$

The tensor Ω_{ij} is the mean rotation tensor. The LRR model can be shown to follow from Lumley's general expression when nonlinear terms in b_{ij} are neglected, i.e., when all coefficients except a_0, a_2, a_7 and a_9 are zero.

A similar, but simpler, nonlinear model has been postulated by Speziale, Sarkar and Gatski (1991). For incompressible flows, this model, known as the **SSG** model, is as follows.

SSG Pressure-Strain Model:

$$\Pi_{ij} = - \left(C_1 \rho \epsilon + C_1^* \tau_{mn} \frac{\partial U_m}{\partial x_n} \right) b_{ij} + C_2 \rho \epsilon \left(b_{ik} b_{kj} - \frac{1}{3} b_{mn} b_{nm} \delta_{ij} \right)$$

$$+ \left(C_3 - C_3^* \sqrt{II} \right) \rho k S_{ij} + C_4 \rho k \left(b_{ik} S_{jk} + b_{jk} S_{ik} - \frac{2}{3} b_{mn} S_{mn} \delta_{ij} \right)$$

$$+ C_5 \rho k (b_{ik} \Omega_{jk} + b_{jk} \Omega_{ik}) \qquad (6.58)$$

$$\left. \begin{array}{llll} C_1 = 3.4, & C_1^* = 1.8, & C_2 = 4.2, & C_3 = 0.8 \\ C_3^* = 1.3, & C_4 = 1.25, & C_5 = 0.4 \end{array} \right\} \qquad (6.59)$$

Interestingly, the SSG model does not appear to require a correction for the pressure-echo effect in order to obtain a satisfactory log-layer solution.

Finally, combining Equations (6.47) through (6.51), we arrive at the well-known LRR model for the rapid pressure strain.

LRR Rapid Pressure-Strain Model:

$$M_{ijkl}\frac{\partial U_k}{\partial x_l} = -\hat{\alpha}\left(P_{ij} - \frac{1}{3}P_{kk}\delta_{ij}\right) - \hat{\beta}\left(D_{ij} - \frac{1}{3}D_{kk}\delta_{ij}\right) - \hat{\gamma}\rho k S_{ij} \quad (6.52)$$

$$P_{ij} = \tau_{im}\frac{\partial U_j}{\partial x_m} + \tau_{jm}\frac{\partial U_i}{\partial x_m} \quad \text{and} \quad D_{ij} = \tau_{im}\frac{\partial U_m}{\partial x_j} + \tau_{jm}\frac{\partial U_m}{\partial x_i} \quad (6.53)$$

$$\hat{\alpha} = \frac{8 + C_2}{11}, \quad \hat{\beta} = \frac{8C_2 - 2}{11}, \quad \hat{\gamma} = \frac{60C_2 - 4}{55}, \quad 0.4 < C_2 < 0.6 \quad (6.54)$$

Note that for compressible flows, the mean strain-rate tensor, S_{ij}, is usually replaced by $S_{ij} - \frac{1}{3}S_{kk}\delta_{ij}$ in Equation (6.52).

One of the most remarkable features of this closure approximation is the presence of just one undetermined closure coefficient, namely, C_2. The value of C_2 has been established by comparison of model predictions with measured properties of homogeneous turbulent flows. Launder, Reece and Rodi (1975) suggested using $C_2 = 0.40$. Morris (1984) revised its value upward to $C_2 = 0.50$, while Launder (1992) currently recommends $C_2 = 0.60$. Section 6.4 discusses the kind of flows used to calibrate this model.

Bradshaw (1973b) has shown that there is an additional contribution to Equations (6.43) and (6.44) that has a nontrivial effect close to a solid boundary. It is attributed to a surface integral that appears in the Green's function for Equation (6.38). This has come to be known as the **pressure-echo effect** or **wall-reflection effect**. Launder, Reece and Rodi (1975) propose a near-wall correction to their model for Π_{ij} that explicitly involves distance from the surface. Gibson and Launder (1978) and Craft and Launder (1992) propose alternative models to account for the pressure-echo effect. For example, the LRR wall-reflection term, $\Pi_{ij}^{(w)}$, is

$$\Pi_{ij}^{(w)} = \left[0.125\frac{\epsilon}{k}(\tau_{ij} + \frac{2}{3}\rho k\delta_{ij}) - 0.015(P_{ij} - D_{ij})\right]\frac{k^{3/2}}{\epsilon n} \quad (6.55)$$

where n is distance normal to the surface.

More recent efforts at devising a suitable closure approximation for Π_{ij} have focused on developing a nonlinear expansion in terms of the anisotropy tensor, b_{ij}, defined in Equation (6.33). Lumley (1978) has systematically developed a general representation for Π_{ij} based on Equations (6.38) through (6.44). In addition to insisting upon coordinate invariance and other required symmetries, Lumley insists upon **realizability**. As noted earlier, this means that all quantities known to be strictly positive must be

guaranteed to be positive by the closure model. Additionally, all computed correlation coefficients must lie between ± 1. This limits the possible form of the functional expansion for Π_{ij}. Lumley argues that the most general form of the complete tensor Π_{ij} for incompressible flow is as follows.

Lumley Pressure-Strain Model:

$$\Pi_{ij} = a_0 \rho \epsilon b_{ij} + a_1 \rho \epsilon \left(b_{ik} b_{jk} - \frac{1}{3} II \delta_{ij} \right) + a_2 \rho k S_{ij}$$

$$+ \rho k \left(a_3 b_{kl} S_{lk} + a_4 b_{kl} b_{lm} S_{mk} \right) b_{ij}$$

$$+ \rho k \left(a_5 b_{kl} S_{lk} + a_6 b_{kl} b_{lm} S_{mk} \right) \left(b_{ik} b_{kj} - \frac{1}{3} II \delta_{ij} \right)$$

$$+ a_7 \rho k \left(b_{ik} S_{jk} + b_{jk} S_{ik} - \frac{2}{3} b_{kl} S_{lk} \delta_{ij} \right)$$

$$+ a_8 \rho k \left(b_{ik} b_{kl} S_{jl} + b_{jk} b_{kl} S_{il} - \frac{2}{3} b_{kl} b_{lm} S_{mk} \delta_{ij} \right)$$

$$+ a_9 \rho k \left(b_{ik} \Omega_{jk} + b_{jk} \Omega_{ik} \right) + a_{10} \rho k \left(b_{ik} b_{kl} \Omega_{jl} + b_{jk} b_{kl} \Omega_{il} \right) \tag{6.56}$$

The eleven closure coefficients are assumed to be functions of the **tensor invariants** II and III, i.e.,

$$a_i = a_i(II, III), \quad II = b_{ij} b_{ij}, \quad III = b_{ik} b_{kl} b_{li} \tag{6.57}$$

The tensor Ω_{ij} is the mean rotation tensor. The LRR model can be shown to follow from Lumley's general expression when nonlinear terms in b_{ij} are neglected, i.e., when all coefficients except a_0, a_2, a_7 and a_9 are zero.

A similar, but simpler, nonlinear model has been postulated by Speziale, Sarkar and Gatski (1991). For incompressible flows, this model, known as the **SSG** model, is as follows.

SSG Pressure-Strain Model:

$$\Pi_{ij} = - \left(C_1 \rho \epsilon + C_1^* \tau_{mn} \frac{\partial U_m}{\partial x_n} \right) b_{ij} + C_2 \rho \epsilon \left(b_{ik} b_{kj} - \frac{1}{3} b_{mn} b_{nm} \delta_{ij} \right)$$

$$+ \left(C_3 - C_3^* \sqrt{II} \right) \rho k S_{ij} + C_4 \rho k \left(b_{ik} S_{jk} + b_{jk} S_{ik} - \frac{2}{3} b_{mn} S_{mn} \delta_{ij} \right)$$

$$+ C_5 \rho k (b_{ik} \Omega_{jk} + b_{jk} \Omega_{ik}) \tag{6.58}$$

$$\left. \begin{array}{l} C_1 = 3.4, \quad C_1^* = 1.8, \quad C_2 = 4.2, \quad C_3 = 0.8 \\ C_3^* = 1.3, \quad C_4 = 1.25, \quad C_5 = 0.4 \end{array} \right\} \tag{6.59}$$

Interestingly, the SSG model does not appear to require a correction for the pressure-echo effect in order to obtain a satisfactory log-layer solution.

Many other proposals have been made for closing the Reynolds-stress equation, with most of the attention on Π_{ij}. Weinstock (1981), Shih and Lumley (1985), Haworth and Pope (1986), Reynolds (1987), Shih, Mansour and Chen (1987), Fu, Launder and Tselepidakis (1987) and Craft et al. (1989) have formulated nonlinear pressure-strain correlation models. As with the k-ϵ model, low-Reynolds-number damping functions are needed to integrate through the sublayer when the ϵ equation is used. Damping functions appear in the pressure-strain correlation tensor as well as in the dissipation. So et al. (1991) give an excellent review of second-order closure models including low-Reynolds-number corrections. Compressibility, of course, introduces an extra complication, and a variety of new proposals are being developed.

While the discussion in this subsection is by design brief, it illustrates the nature of the closure problem for second-order closure models. Although dimensional analysis combined with physical insight still plays a role, there is a greater dependence upon the formalism of tensor calculus. To some extent, this approach focuses more on the differential equations than on the physics of turbulence. This appears to be necessary because the increased complexity mandated by having to model second and higher rank tensors makes it difficult to intuit the proper forms solely on the strength of physical reasoning. Fortunately, the arguments developed during the past decade have a stronger degree of rigor than the drastic surgery approach to modeling terms in the dissipation-rate equation discussed in Subsection 4.3.2.

6.3.2   Launder-Reece-Rodi Model

The model devised by Launder, Reece and Rodi (1975) is the most well known and most thoroughly tested second-order closure model based on the ϵ equation. Most newer second-order closure models are based on the LRR model and differ primarily in the closure approximation chosen for Π_{ij}. Combining the closure approximations discussed in the preceding subsection, we have the following high-Reynolds-number form of the model.

Reynolds-Stress Tensor

$$\frac{\partial \tau_{ij}}{\partial t} + \frac{\partial}{\partial x_k}\left(U_k \tau_{ij}\right) = -P_{ij} + \frac{2}{3}\rho\epsilon\delta_{ij} - \Pi_{ij} \cdot$$
$$-C_s \frac{\partial}{\partial x_k}\left[\frac{k}{\epsilon}\left(\tau_{im}\frac{\partial \tau_{jk}}{\partial x_m} + \tau_{jm}\frac{\partial \tau_{ik}}{\partial x_m} + \tau_{km}\frac{\partial \tau_{ij}}{\partial x_m}\right)\right] \quad (6.60)$$

Dissipation Rate

$$\rho\frac{\partial \epsilon}{\partial t} + \rho U_j \frac{\partial \epsilon}{\partial x_j} = C_{\epsilon 1}\frac{\epsilon}{k}\tau_{ij}\frac{\partial U_i}{\partial x_j} - C_{\epsilon 2}\rho\frac{\epsilon^2}{k} - C_\epsilon\frac{\partial}{\partial x_k}\left[\frac{k}{\epsilon}\tau_{km}\frac{\partial \epsilon}{\partial x_m}\right] \quad (6.61)$$

Pressure-Strain Correlation

$$\Pi_{ij} = C_1\frac{\epsilon}{k}\left(\tau_{ij} + \frac{2}{3}\rho k\delta_{ij}\right) - \hat{\alpha}\left(P_{ij} - \frac{2}{3}P\delta_{ij}\right)$$

$$-\hat{\beta}\left(D_{ij} - \frac{2}{3}P\delta_{ij}\right) - \hat{\gamma}\rho k\left(S_{ij} - \frac{1}{3}S_{kk}\delta_{ij}\right)$$

$$+\left[0.125\frac{\epsilon}{k}(\tau_{ij} + \frac{2}{3}\rho k\delta_{ij}) - 0.015(P_{ij} - D_{ij})\right]\frac{k^{3/2}}{\epsilon\,n} \quad (6.62)$$

Auxiliary Relations

$$P_{ij} = \tau_{im}\frac{\partial U_j}{\partial x_m} + \tau_{jm}\frac{\partial U_i}{\partial x_m}, \quad D_{ij} = \tau_{im}\frac{\partial U_m}{\partial x_j} + \tau_{jm}\frac{\partial U_m}{\partial x_i}, \quad P = \frac{1}{2}P_{kk}$$
$$(6.63)$$

Closure Coefficients [Launder (1992)]

$$\left.\begin{array}{lll} \hat{\alpha} = (8 + C_2)/11, & \hat{\beta} = (8C_2 - 2)/11, & \hat{\gamma} = (60C_2 - 4)/55 \\ C_1 = 1.8, & C_2 = 0.60, & C_s = 0.11 \\ C_\epsilon = 0.18, & C_{\epsilon 1} = 1.44, & C_{\epsilon 2} = 1.92 \end{array}\right\} \quad (6.64)$$

Note that Equation (6.61) differs from the ϵ equation used with the Standard k-ϵ model [Equation (4.42)] in the form of the diffusion term. Rather than introduce the eddy viscosity, Launder, Reece and Rodi opt to use the analog of the turbulent transport term, C_{ijk}. The values of the closure coefficients in Equation (6.64) are specific to the LRR model of course, and their values are influenced by the specific form assumed for Π_{ij}. In their original paper, Launder, Reece and Rodi recommend $C_1 = 1.5$, $C_2 = 0.4$, $C_s = 0.11$, $C_\epsilon = 0.15$, $C_{\epsilon 1} = 1.44$ and $C_{\epsilon 2} = 1.90$. The values quoted in Equation (6.64) are those currently recommended by Launder (1992).

6.3.3   Wilcox Multiscale Model

Not all second-order closure models use the ϵ equation to compute ϵ. Wilcox and Rubesin (1980) postulate a second-order closure model based on their ω^2 equation and the LRR model for Π_{ij}. Although the model showed some promise for flows over curved surfaces and for swirling flows, its applications were very limited. By contrast, Wilcox (1988b) proposes a second-order closure model that has had a wide range of applications.

The model, known as the multiscale model, has some novel features that are worthy of mention. The model was intended to serve as an improved algebraic stress model. The intended improvement was to include real time dependent convective terms rather than using Rodi's Equation (6.22).

To accomplish this end, the model idealizes turbulent flows as consisting of two distinct types of eddies. The first type are large, or upper partition, eddies that contain most of the turbulence energy and primarily transport the Reynolds stresses. The second are small, or lower partition, eddies that are isotropic and primarily dissipative. The kinetic energy of the small eddies is e so that the kinetic energy of the large eddies is $k - e$. This notion is used in Large Eddy Simulation work (see Chapter 8) where small eddies (corresponding to the lower partition of the spectrum) are modeled and large eddies (corresponding to the upper partition of the spectrum) are numerically simulated. Both types of eddies are modeled in the multiscale model.

The model consists of a tensor equation governing the development of the small and large eddies, including an energy exchange process that governs their interaction. Because of the assumed form of the equations, the exchange tensor is essentially the pressure-strain correlation tensor, Π_{ij}. The model uses the LRR pressure-strain model, although the formulation is sufficiently general to permit the use of any plausible pressure-strain formulation.

Using a series of physical arguments, Wilcox arrives at a closed set of equations that can be combined to yield an equation for the Reynolds-stress tensor. Although the formulation differs in spirit from the conventional term-by-term closure approach, the model effectively uses the Kolmogorov (1941) hypothesis of local isotropy for the lower partition, while the effective closure approximation for C_{ijk} is given by

$$C_{ijk} + \nu \frac{\partial \tau_{ij}}{\partial x_k} \approx -\frac{2}{3} \left(\mu + \sigma^* \mu_T \right) \frac{\partial k}{\partial x_k} \delta_{ij} \qquad (6.65)$$

This equation is the approximation that replaces Rodi's ASM approximation. The most important consequence is that the turbulent transport of the shear stresses is neglected. This is consistent with the idealized notion that the large eddies move in an inviscid manner. Computationally, most notably in boundary-layer computations, the multiscale model often behaves very much like an ASM. Using standard notation, the Wilcox multiscale model is as follows.

Reynolds-Stress Tensor

$$\frac{\partial \tau_{ij}}{\partial t} + \frac{\partial}{\partial x_k}(U_k \tau_{ij}) = -P_{ij} + \frac{2}{3}\beta^* \rho \omega k \delta_{ij} - \Pi_{ij}$$
$$-\frac{2}{3}\frac{\partial}{\partial x_k}\left[(\mu + \sigma^* \mu_T)\frac{\partial k}{\partial x_k}\delta_{ij}\right] \tag{6.66}$$

Specific Dissipation Rate

$$\rho \frac{\partial \omega}{\partial t} + \rho U_j \frac{\partial \omega}{\partial x_j} = \alpha \frac{\omega}{k}\tau_{ij}\frac{\partial U_i}{\partial x_j} - \beta \rho \omega \left[\omega + \hat{\xi}\sqrt{2\Omega_{mn}\Omega_{mn}}\right]$$
$$+\frac{\partial}{\partial x_k}\left[(\mu + \sigma \mu_T)\frac{\partial \omega}{\partial x_k}\right] \tag{6.67}$$

Upper Partition Energy

$$\rho\frac{\partial(k-e)}{\partial t} + \rho U_j \frac{\partial(k-e)}{\partial x_j} = \left(1 - \hat{\alpha} - \hat{\beta}\right)P - \beta^* \rho \omega k \left(1 - \frac{e}{k}\right)^{3/2} \tag{6.68}$$

Pressure-Strain Correlation

$$\Pi_{ij} = \beta^* C_1 \omega \left(\tau_{ij} + \frac{2}{3}\rho k \delta_{ij}\right) - \hat{\alpha}\left(P_{ij} - \frac{2}{3}P\delta_{ij}\right)$$
$$-\hat{\beta}\left(D_{ij} - \frac{2}{3}P\delta_{ij}\right) - \hat{\gamma}\rho k \left(S_{ij} - \frac{1}{3}S_{kk}\delta_{ij}\right) \tag{6.69}$$

Auxiliary Relations

$$\mu_T = \rho k/\omega \tag{6.70}$$

$$P_{ij} = \tau_{im}\frac{\partial U_j}{\partial x_m} + \tau_{jm}\frac{\partial U_i}{\partial x_m}, \quad D_{ij} = \tau_{im}\frac{\partial U_m}{\partial x_j} + \tau_{jm}\frac{\partial U_m}{\partial x_i}, \quad P = \frac{1}{2}P_{kk} \tag{6.71}$$

Closure Coefficients

$$\left.\begin{array}{l} \alpha = 4/5, \quad \beta = 3/40, \quad \beta^* = 9/100, \quad \sigma = 1/2, \quad \sigma^* = 1/2 \\ \hat{\alpha} = 42/55, \quad \hat{\beta} = 6/55, \quad \hat{\gamma} = 1/4, \quad \hat{\xi} = 1 \\ C_1 = 1 + 4(1 - e/k)^{3/2} \end{array}\right\} \tag{6.72}$$

The term proportional to $\hat{\xi}$ in Equation (6.67) is the only formal difference from the k-ω model's Equation (4.35). Because of this term, the value of α must increase from 5/9 to 4/5. All other closure coefficients shared by the k-ω and multiscale models have the same values. The term proportional to $\hat{\xi}$ follows from the LES work of Bardina, Ferziger and Reynolds (1983). In the context of homogeneous turbulence, it is required to accurately simulate effects of system rotation. The term also introduces subtle differences

between model-predicted effects of plane strain and uniform shear on homogeneous turbulence.

Note that the values chosen for $\hat{\alpha}$ and $\hat{\beta}$ are those used in the original Launder, Reece and Rodi (1975) model. However, a modified value of $1/4$ rather than the LRR value of $4/11$ has been selected for $\hat{\gamma}$ to optimize model predictions for homogeneous turbulence. Also, in a the log layer of a flat-plate boundary layer, the model predicts $e/k \approx 0.75$ so that the value of C_1 is 1.5. This matches the value used in the original LRR model.

6.4 Application to Homogeneous Turbulent Flows

Homogeneous turbulent flows are useful for establishing the new closure coefficients introduced in modeling the pressure-strain correlation tensor, Π_{ij}. This is the primary type of flow normally used to calibrate a second-order closure model. Recall that homogeneous turbulence is defined as a turbulent flow that, on the average, is uniform in all directions. This means the diffusion terms in all of the equations of motion are identically zero, as is the pressure-echo correction. Hence, the primary remaining difference between the LRR and Wilcox multiscale models when applied to homogeneous turbulent flows is in the scale-determining equation. That is, both models use the LRR pressure-strain model and the Kolmogorov isotropy hypothesis, so that the equations for the Reynolds stresses are nearly identical. The only differences are: (a) the LRR model uses the ϵ equation while the multiscale model uses the ω equation; and, (b) the closure coefficient C_1 is constant for the LRR model while it varies with large-eddy energy, $(k - e)$, for the multiscale model.

Additionally, since the diffusion terms vanish, the equations simplify to first-order, ordinary differential equations, which can sometimes be solved in closed form. At worst, a simple Runge-Kutta integration is required. Such flows are ideal for helping establish values of closure coefficients such as C_1 and C_2 in the LRR model, provided of course that we believe the same values apply to all turbulent flows.

The simplest of all homogeneous flows is the decay of isotropic turbulence. We discussed homogeneous isotropic turbulence in Section 4.4, and established the ratio of β^* to β for the k-ω model. The multiscale model equations for k and ω simplify to

$$\frac{dk}{dt} = -\beta^* \omega k \quad \text{and} \quad \frac{d\omega}{dt} = -\beta \omega^2 \qquad (6.73)$$

For large time, the asymptotic solution for k is given by

$$k \sim t^{-\beta^*/\beta} \tag{6.74}$$

Similarly, for the LRR model, k varies with t according to

$$k \sim t^{-1/(C_{\epsilon 2}-1)} \tag{6.75}$$

Experimental observations summarized by Townsend (1976) indicate that $k \sim t^{-n}$ where $n = 1.25 \pm 0.06$ for decaying homogeneous, isotropic turbulence. Hence, we can conclude that our closure coefficients must lie in the following ranges.

$$1.19 < \beta^*/\beta < 1.31, \quad 1.76 < C_{\epsilon 2} < 1.84 \tag{6.76}$$

Figures 6.4(a) and (b) compare computed and measured k for decaying homogeneous, isotropic turbulence as predicted by the Wilcox multiscale model. The experimental data in (a) and (b) are those of Comte-Bellot and Corrsin (1971) and Wigeland and Nagib (1978), respectively.

The second type of homogeneous turbulent flow that is useful for establishing the value of pressure-strain correlation closure coefficients is decaying anisotropic turbulence. Assuming dissipation follows the Kolmogorov (1941) isotropy hypothesis [Equation (6.30)], and using Rotta's (1951) slow pressure-strain term [Equation (6.45)], the Reynolds-stress equation is

$$\frac{d\tau_{ij}}{dt} = \frac{2}{3}\rho\epsilon\delta_{ij} - C_1\frac{\epsilon}{k}\left(\tau_{ij} + \frac{2}{3}\rho k\delta_{ij}\right) \tag{6.77}$$

The solution is readily shown to be

$$\tau_{ij} + \frac{2}{3}\rho k\delta_{ij} = \left(\tau_{ij} + \frac{2}{3}\rho k\delta_{ij}\right)_o \left(\frac{k_o\epsilon}{k\epsilon_o}\right)^{C_1/(C_{\epsilon 2}-1)} \tag{6.78}$$

where subscript o denotes initial value. The experimental data of Uberoi (1956) indicate that the coefficient C_1 lies in the range

$$1.4 < C_1 < 1.8 \tag{6.79}$$

Figures 6.4(e), (f), (g) and (h) compare computed k and normal Reynolds stresses with Uberoi's measurements for decaying homogeneous, anisotropic turbulence as predicted by the Wilcox multiscale model.

Note that C_1 is not a constant in the multiscale model, but instead varies with e/k. The range of values for C_1 in Equation (6.79) correspond to e/k lying in the range $0.66 < e/k < 0.78$. This is inconsistent with
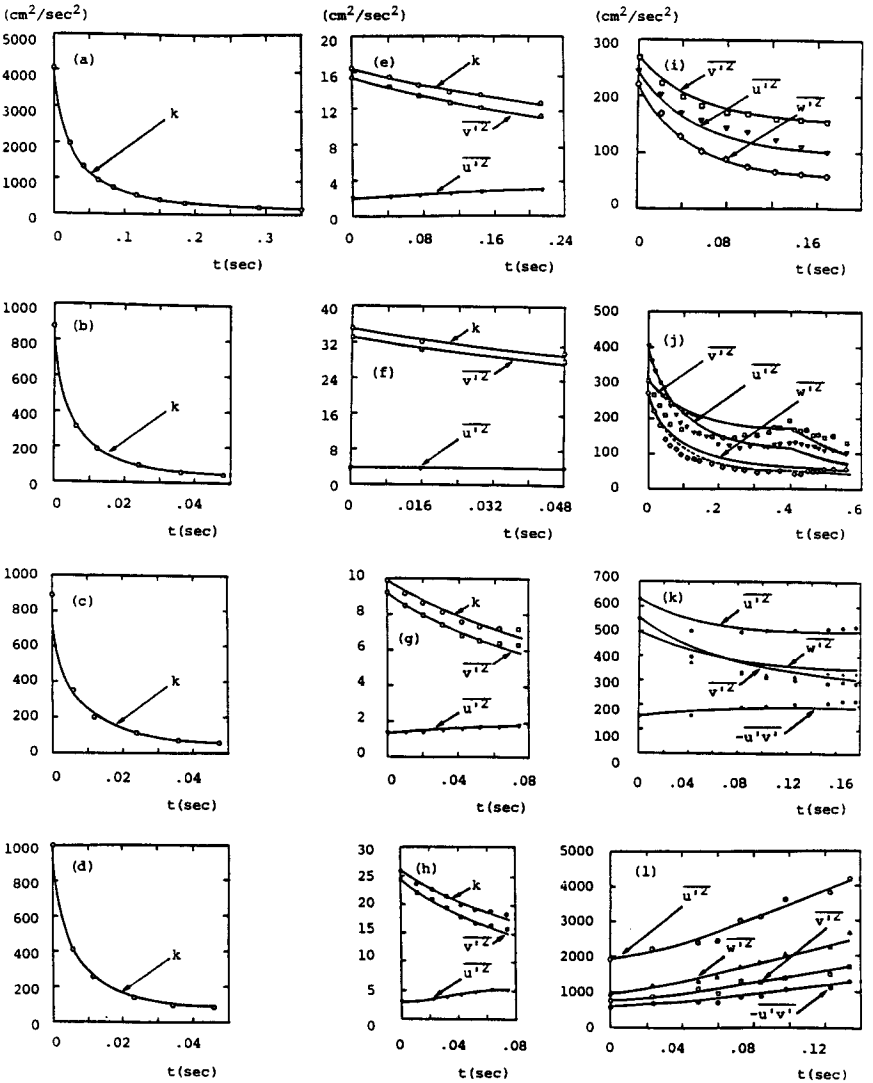
Figure 6.4: Computed and measured turbulence energy and Reynolds stresses for homogeneous turbulent flows; —— Wilcox multiscale model; ○ ● □ △ ▽ measured. [From Wilcox (1988b) — Copyright © AIAA 1988 — Used with permission.]

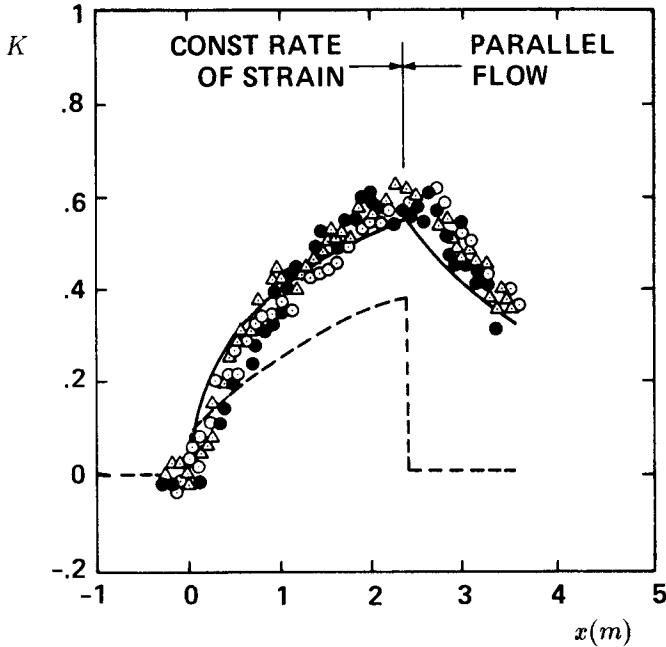Figure 6.5: Computed and measured distortion parameter for the Tucker-Reynolds plane-strain flow; - - - Wilcox-Rubesin k-ω^2 model; —— Wilcox-Rubesin second-order closure model; ○ ● △ Tucker-Reynolds. [From Wilcox and Rubesin (1980).]

Kolmogorov's notion that the large eddies contain most of the energy, and represents a conceptual flaw in the multiscale model. However, virtually all multiscale applications have been done using values of e/k that correspond to C_1 lying in the range quoted in Equation (6.79). The model's predictions are not strongly affected by simply using a constant value of C_1 and dropping Equation (6.68).

To illustrate how much of an improvement second-order closure models make for flows with sudden changes in mean strain rate, Figure 6.5 compares measured distortion parameter, K, for the Tucker-Reynolds experiment with computed results obtained using the Wilcox-Rubesin (1980) k-ω^2 and second-order closure models. As shown, the second-order closure model predicts a gradual approach to isotropy and the computed K more closely matches the experimental data.

Figure 6.6 compares computed and measured normal components of the Reynolds-stress anisotropy tensor, b_{ij}, for the experiment conducted by

Choi and Lumley (1984). This experiment is similar to the Tucker-Reynolds experiment, with turbulence initially subjected to plain strain and then returning to isotropy after the strain is removed. This computation has been done with the original LRR model using $C_1 = 1.5$.
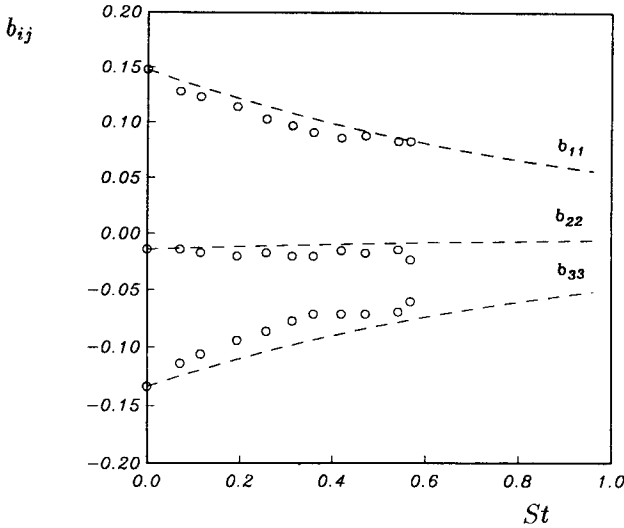

Figure 6.6: Comparison of computed and measured anisotropy tensor for decaying homogeneous, anisotropic turbulence; - - - LRR model; o Choi and Lumley. [From Speziale (1991) — Published with permission of author.]

While discrepancies between computed and measured stresses are satisfactory, even closer agreement between theory and experiment can be obtained with a nonlinear model for the slow pressure-strain model. Sarkar and Speziale (1990), for example, propose a simple quadratic model for the slow pressure-strain given by

$$A_{ij} = -C_1\rho\epsilon b_{ij} + C_2\rho\epsilon \left(b_{ik}b_{kj} - \frac{1}{3}b_{mn}b_{nm}\delta_{ij} \right) \qquad (6.80)$$

where $C_1 = 3.4$ and $C_2 = 4.2$ [see Equation (6.58)]. Figure 6.7 compares the so-called **phase-space portrait** of the return-to-isotropy problem. The figure shows the variation of the second tensor invariant $II = b_{ij}b_{ji}$ as a function of the third tensor invariant, $III = b_{ik}b_{kl}b_{li}$. The nonlinear model clearly falls within the scatter of the experimental data, while the LRR model prediction provides a less satisfactory description.
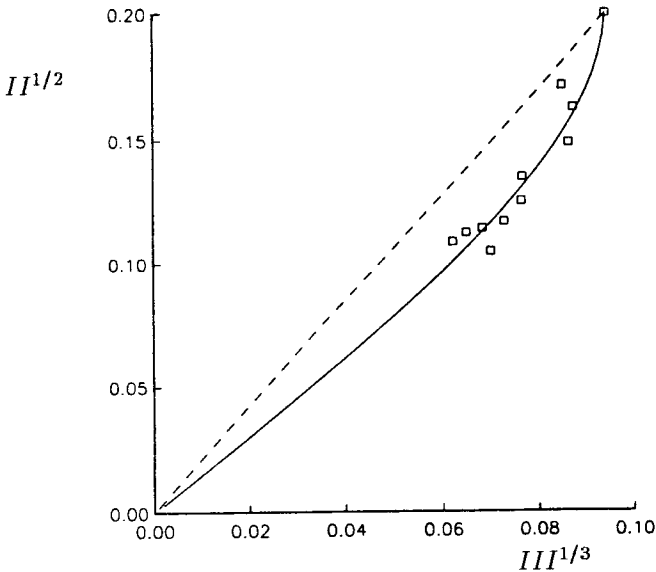
Figure 6.7: Phase-space portrait for decaying homogeneous, anisotropic turbulence; - - - LRR model; —— Sarkar-Speziale model; □ Choi and Lumley. [From Speziale (1991) — Published with permission of author.]

Homogeneous turbulence experiments have also been performed that include irrotational plane strain [Townsend (1956) and Tucker and Reynolds (1968)] and uniform shear [Champagne, Harris and Corrsin (1970), Harris, Graham and Corrsin (1977), Tavoularis and Corrsin (1981), and Tavoularis and Karnik (1989)]. These flows can be used to establish closure coefficients such as C_2 in the LRR pressure-strain model. The velocity gradient tensor for these flows is:

$$\frac{\partial U_i}{\partial x_j} = \begin{bmatrix} 0 & S & 0 \\ 0 & -a & 0 \\ 0 & 0 & a \end{bmatrix} \tag{6.81}$$

where a is the constant strain rate and S is the constant rate of mean shear.

While closed form solutions generally do not exist when mean strain rate and/or shear are present, analytical progress can be made for the asymptotic forms in the limit $t \to \infty$. In general, the specific dissipation rate, $\omega \sim \epsilon/k$, approaches a constant limiting value while k and the Reynolds stresses grow exponentially. Assuming solutions of this form yields closed-form expressions for the Reynolds stresses.

Using such analysis for uniform shear ($a = 0, S \neq 0$), Abid and Speziale (1992) have analyzed the LRR and SSG pressure-strain models and two new nonlinear pressure-strain models developed by Shih and Lumley (1985) [SL model] and by Fu, Launder and Tselepidakis (1987) [FLT model]. Table 6.1 summarizes their results, along with results for the multiscale model (MS) and asymptotic values determined experimentally by Tavoularis and Karnik (1989). As shown, the SSG model most faithfully reproduces measured asymptotic values of the Reynolds stresses. Note that the multiscale model's modified value for $\hat{\gamma}$ in the LRR rapid pressure-strain model yields a closer match to the measured b_{xy} than the original LRR model, while MS and LRR normal components are nearly identical.

Table 6.1: Anisotropy-Tensor Limiting Values for Uniform Shear

Property	MS	LRR	SL	FLT	SSG	Measured
b_{xx}	.156	.152	.120	.196	.218	.210
b_{xy}	-.154	-.186	-.121	-.151	-.164	-.160
b_{yy}	-.122	-.119	-.122	-.136	-.145	-.140
b_{zz}	-.034	-.033	.002	-.060	-.073	-.070
Sk/ϵ	4.965	4.830	7.440	5.950	5.500	5.000

Figure 6.4(k) compares multiscale model Reynolds stresses with corresponding measured values for the Champagne, Harris and Corrsin (1970) uniform-shear experiment with $S = 12.9$ sec^{-1}. Figure 6.4(l) makes a similar comparison with the measurements of Harris, Graham and Corrsin (1977) for which $S = 48.0$ sec^{-1}. For both flows, the asymptotic value of e/k is 4/5. Both computations use $(e/k)_o = 4/5$.

Turning to flows with irrotational strain rate ($a \neq 0, S = 0$), Figure 6.4(i) and (j) compare multiscale model and measured [Townsend (1956) and Tucker and Reynolds (1968), respectively] k and Reynolds stresses. The strain rate for the Townsend case is $a = 9.44$ sec^{-1}, while the Tucker-Reynolds case has $a = 4.45$ sec^{-1}. Launder, Reece and Rodi (1975) report very similar results for the Tucker-Reynolds case. The multiscale model results are mildly sensitive to the initial value of e/k. Both cases have been done using $(e/k)_o = 3/4$, which turns out to be the long-time asymptotic value predicted by the model for uniform strain rate. Varying the initial ratio between 1/2 and 9/10 produces less than a 15% change overall in the Reynolds stresses. Figure 6.4(j) shows the results obtained for the Tucker-Reynolds case using initial e/k ratios of 3/4 (solid curves) and 9/10 (dashed

curves). As shown, the primary difference appears in $\overline{w'^2}$. Using the larger value produces closer agreement between theory and experiment.

Rotating homogeneous turbulent flow is of some interest as it includes Coriolis and centrifugal accelerations. The experiments of Wigeland and Nagib (1978), for example, involve decaying axisymmetric homogeneous turbulence that is subjected to constant angular rotation rate, Ω. Figures 6.4(b), (c) and (d) compare computed and measured k for rotation rates of 0, 20 sec^{-1} and 80 sec^{-1}, respectively. These computations have been used to establish the value of $\hat{\xi}$ in the Wilcox multiscale model. As noted earlier, this term was borrowed from the LES work of Bardina, Ferziger and Reynolds (1983). Speziale (1991) indicates that the nonlinear SSG pressure-strain model precludes the need for such rotation dependent terms in the ϵ or ω equation.

6.5 Application to Free Shear Flows

While second-order closure models eliminate many of the shortcomings of the Boussinesq eddy-viscosity approximation, they do not appear to solve the free shear flow problem. Table 6.2 summarizes computed and measured spreading rates for the Wilcox multiscale model and the LRR model. As shown in the table, while the multiscale model displays much less sensitivity to the freestream value of ω than the k-ω model (see Table 4.2), its spreading rate is somewhat smaller than measured for the far wake. The LRR model's spreading rates are roughly 10% larger than those of the Standard k-ϵ model. As noted by Launder and Morse (1979), because the predicted round-jet spreading rate exceeds the predicted plane-jet spreading rate, the LRR model fails to resolve the round-jet/plane-jet anomaly.

Table 6.2: Free Shear Flow Spreading Rate

Flow	Multiscale Model	LRR Model	Measured
Far Wake	.248-.292	—	.365
Mixing Layer	.102-.115	.104	.115
Plane Jet	—	.123	.100-.110
Round Jet	—	.135	.086-.095

Figure 6.8 compares computed and measured width of a curved mixing layer. The computation was done using the LRR model [Rodi (1981)], and the measurements correspond to an experiment of Castro and Bradshaw

(1976) with stabilizing curvature. As shown, the LRR model predicts a greater reduction in width than the Standard k-ϵ model. However, the LRR model's predicted width lies as far below the measured width as the k-ϵ model's prediction lies above. Although not shown in the figure, Rodi's (1976) Algebraic Stress Model predicts a width about midway between, and thus in close agreement with measured values.
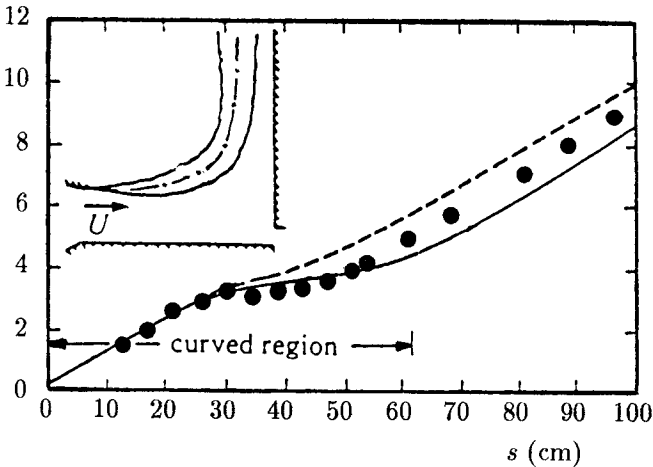
δ (cm)

Figure 6.8: Comparison of computed and measured width for a curved mixing layer; —— LRR model; - - - Standard k-ϵ model; ● Castro and Bradshaw. [From Rodi (1981) — Copyright © AIAA 1981 — Used with permission.]

As a final comment, with all of the additional new closure coefficients attending nonlinear pressure-strain models, it is very likely that such models can be fine tuned to correct the round-jet/plane-jet anomaly. However, we should keep in mind that the anomaly underscores a deficiency in our physical description and understanding of jets. Be aware that such fine tuning reveals nothing regarding the nature of these flows, and thus amounts to little more than a curve-fitting exercise.

6.6   Application to Wall-Bounded Flows

This section focuses upon wall-bounded flows, including channel and pipe flow, and boundary layers with a variety of complicating effects. Before

addressing such flows, however, we discuss surface boundary conditions. As with two-equation models, we have the option of using wall functions or integrating through the viscous sublayer.

6.6.1   Surface Boundary Conditions

Wall-bounded flows require boundary conditions appropriate to a solid boundary for the mean velocity and the scale-determining parameter, e.g., ϵ or ω. Additionally, surface boundary conditions are needed for each component of the Reynolds-stress tensor (implying a boundary condition for k). The exact surface boundary conditions follow from the no-slip condition:

$$\tau_{ij} = 0 \quad \text{at} \quad y = 0 \qquad (6.82)$$

Second-order closure models, like two-equation models, may or may not predict a satisfactory value of the constant B in the law of the wall when the equations are integrated through the viscous sublayer. If the model fails to predict a satisfactory value for B, we have the choice of either introducing viscous damping factors or using wall functions to obviate integration through the sublayer. The near-wall behavior of second-order closure models is strongly influenced by the scale-determining equation. Models based on the ϵ equation fail to predict an acceptable value of B and are very difficult to integrate through the sublayer. By contrast, models based on the ω equation often predict an acceptable value of B and are generally quite easy to integrate through the sublayer.

The most rational procedure for devising wall functions is to analyze the log layer with perturbation methods. As with the k-ϵ model, the velocity, k and either ϵ or ω are given by

$$U = u_\tau \left[\frac{1}{\kappa} \ell n \left(\frac{u_\tau y}{\nu} \right) + B \right] \qquad (6.83)$$

$$k = \frac{u_\tau^2}{\sqrt{\beta^*}}, \qquad \omega = \frac{k^{1/2}}{(\beta^*)^{1/4} \kappa y}, \qquad \epsilon = (\beta^*)^{3/4} \frac{k^{3/2}}{\kappa y} \qquad (6.84)$$

Similar relations are needed for the Reynolds stresses, and the precise forms depend upon the approximations used to close the Reynolds-stress equation. The Problems section examines log-layer structure for the LRR and Wilcox multiscale models. Regardless of the model, the general form of the Reynolds-stress tensor is

$$\tau_{ij} = C_{ij} \rho k \quad \text{as} \quad y \to 0 \qquad (6.85)$$

where C_{ij} is a constant tensor whose components depend upon the model's closure coefficients.

So, Lai, Zhang, and Hwang (1991) review low-Reynolds-number corrections for second-order closure models based on the ϵ equation. The damping functions generally introduced are similar to those proposed for the k-ϵ model (see Section 4.9). As with the k-ϵ model, many authors have postulated low-Reynolds-number·damping functions, and the topic remains in a continuing state of development.

As with the k-ω model, the surface value of specific dissipation rate, ω_w, determines the value of the constant B in the law of the wall for the multiscale model. Perturbation analysis of the sublayer shows that the limit $\omega_w \rightarrow \infty$ corresponds to a perfectly-smooth wall and, without low-Reynolds-number corrections, the asymptotic behavior of ω approaching the surface for both the k-ω and multiscale models is

$$\omega \rightarrow \frac{6\nu_w}{\beta y^2} \quad \text{as} \quad y \rightarrow 0 \quad \text{(Smooth Wall)} \tag{6.86}$$

Using Program SUBLAY (Appendix C), the multiscale model's sublayer behavior can be readily determined. Most importantly, the constant, B, in the law of the wall is

$$B = 5.2 \tag{6.87}$$

Thus, the multiscale model can be integrated through the viscous sublayer without the aid of viscous damping functions. Figure 6.9(a) compares multiscale model smooth-wall velocity profiles with corresponding measurements of Laufer (1952), Andersen, Kays and Moffat (1972), and Wieghardt [as tabulated by Coles and Hirst (1969)]. Figure 6.9(b) compares computed turbulence production and dissipation terms with Laufer's (1952) near-wall pipe-flow measurements. In all cases, predictions are within experimental error bounds.

The multiscale model also has the property that the constant B varies with the surface value of ω. We can thus correlate ω_w with surface roughness height, k_R, and surface mass-injection velocity, v_w. The resulting correlations are a little different from those appropriate for the k-ω model. The surface boundary conditions based on these correlations are as follows.
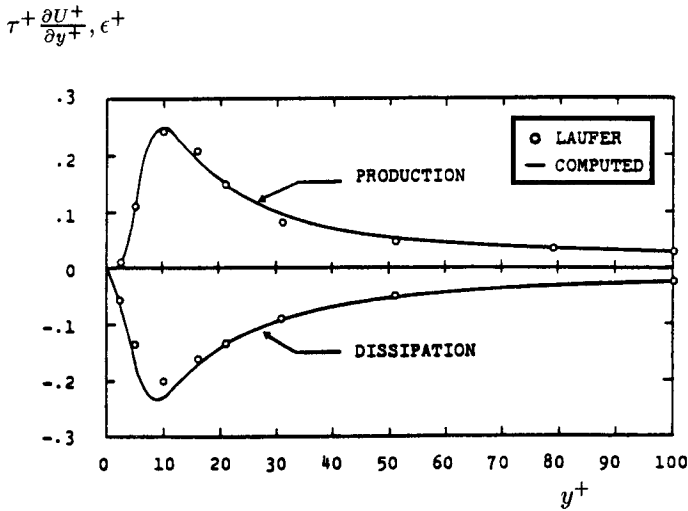
For rough surfaces:

$$\omega = \frac{u_\tau^2 S_R}{\nu_w} \quad \text{at} \quad y = 0 \quad \text{(Rough Wall)} \tag{6.88}$$

where the dimensionless coefficient S_R is defined in terms of $k_R^+ = u_\tau k_R/\nu_w$ by

$$S_R = \begin{cases} (50/k_R^+)^2, & k_R^+ \leq 25 \\[2ex] 500/(k_R^+)^{3/2} & k_R^+ > 25 \end{cases} \tag{6.89}$$

U^+
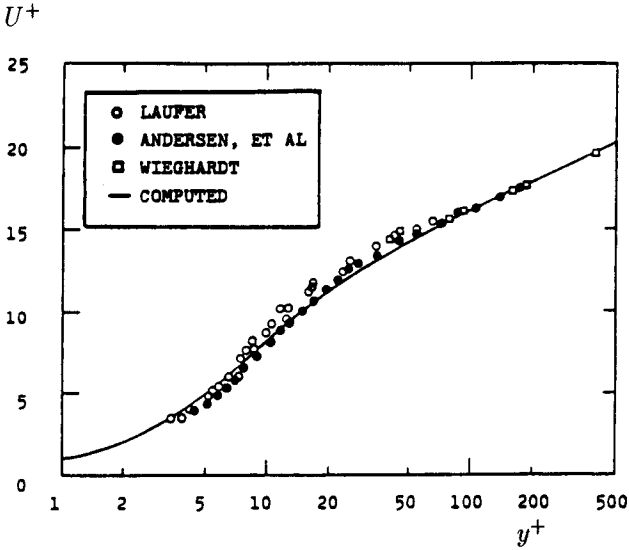
(a) Velocity

$\tau^+ \frac{\partial U^+}{\partial y^+}, \epsilon^+$

(b) Production and dissipation

Figure 6.9: Computed and measured sublayer properties; multiscale model. [From Wilcox (1988b) — Copyright © AIAA 1988 — Used with permission.]

For surfaces with mass injection:

$$\omega = \frac{u_\tau^2 S_B}{\nu_w} \quad \text{at} \quad y = 0 \quad \text{(Mass Injection)} \tag{6.90}$$

where the dimensionless coefficient S_B is defined in terms of $v_w^+ = v_w/u_\tau$ by

$$S_B = \frac{16}{v_w^+(1 + 4v_w^+)} \tag{6.91}$$

As a final comment, while the multiscale model does not require viscous damping functions to achieve a satisfactory sublayer solution, introducing low-Reynolds-number corrections can improve model predictions for a variety of flows. Most importantly, with straightforward viscous damping functions very similar to those introduced for the k-ω model (see Subsection 4.9.2), the model's ability to predict transition can be greatly improved. As with the k-ω model, we let

$$\mu_T = \alpha^* \frac{\rho k}{\omega} \tag{6.92}$$

and the closure coefficients in Equations (6.72) are replaced by the following.

$$\left. \begin{aligned} \alpha^* &= \frac{\alpha_o^* + Re_T/R_k}{1 + Re_T/R_k} \\ \alpha &= \frac{4}{5} \cdot \frac{\alpha_o + Re_T/R_\omega}{1 + Re_T/R_\omega} \\ \beta^* &= \frac{9}{100} \cdot \frac{5/18 + (Re_T/R_\beta)^4}{1 + (Re_T/R_\beta)^4} \\ \hat{\gamma} &= \frac{1}{4} \cdot \frac{\hat{\gamma}_o + Re_T/R_k}{1 + Re_T/R_k} \end{aligned} \right\} \tag{6.93}$$

$$\left. \begin{aligned} \beta &= 3/40, \quad \sigma^* = \sigma = 1/2, \quad \hat{\alpha} = 42/55, \quad \hat{\beta} = 6/55, \quad \hat{\xi} = 1 \\ \alpha_o^* &= \beta/3, \quad \alpha_o = 1/10, \quad \hat{\gamma}_o = 9/500 \\ R_\beta &= 8, \quad R_k = 6, \quad R_\omega = 3/4, \quad C_1 = 1 + 4(1 - e/k)^{3/2} \end{aligned} \right\} \tag{6.94}$$

Note that, unlike the k-ω model, the factor $(\alpha^*)^{-1}$ is not required in the equation for α [see Equation (4.223) for comparison]. With these viscous corrections, the multiscale model reproduces all of the low-Reynolds-number k-ω model transition-predictions discussed in Subsection 4.9.2, and other subtle features such as asymptotic consistency. The values chosen for R_β, R_k and R_ω yield $B = 5.0$.

6.6.2   Channel and Pipe Flow

Figure 6.10 compares computed and measured velocity and Reynolds-stress profiles for the original Launder-Reece-Rodi model. The computation has been done using wall functions. Velocity profile data shown are those of Laufer (1951) and Hanjalić (1970), while the Reynolds-stress data are those of Comte-Bellot (1965). As shown, with the exception of $\overline{u'^2}$, computed and measured profiles differ by less than 5%. The computed and measured $\overline{u'^2}$ profiles differ by no more than 20%. Although not shown, even closer agreement between computed and measured Reynolds stresses can be obtained with low-Reynolds-number versions of the LRR model [see So et al. (1991)].

One of the most controversial features of the LRR model solution for channel flow is the importance of the pressure-echo term throughout the flow. The pressure-echo contribution on the centerline is approximately 15% of its peak value. It is unclear that a supposed near-wall effect should have this large an impact at the channel centerline. However, some researchers argue that the echo effect scales with maximum eddy size which, for channel flow, would be about half the channel height.
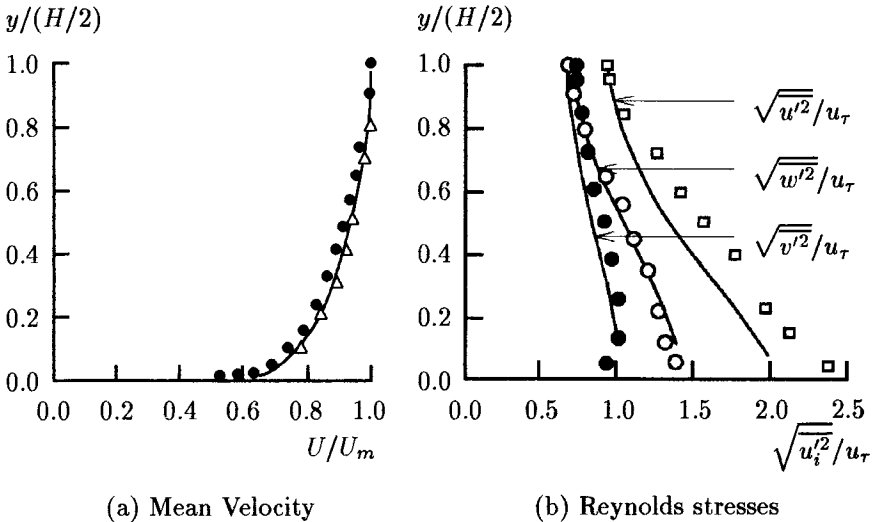

(a) Mean Velocity   (b) Reynolds stresses

Figure 6.10: Computed and measured flow properties for channel flow; —— LRR model; (a) △ Laufer, • Hanjalić; (b) □ ○ • Comte-Bellot.

Figures 6.11 and 6.12 compare computed and measured channel-flow and pipe-flow properties for the multiscale model with and without viscous corrections. As shown, computed skin friction is generally within 3% of the

Halleen and Johnston (1967) correlation [see Equation (3.137)] for channel flow. Similarly, computed c_f differs from Prandtl's universal law of friction [see Equation (3.138)] by less than 3% except at the lowest Reynolds numbers. For both channel and pipe flow, the velocity, Reynolds shear stress, and turbulence kinetic energy profiles differ by less than 6%. Most notably, the low-Reynolds-number model predicts the peak value of k near the wall to within 10% of the DNS value for channel flow and 4% of the measured value for pipe flow. For both cases, the turbulence-energy production, $\tau_{xy}\partial U/\partial y$, and dissipation, ϵ, are within 10% of the DNS and measured results except very close to the surface.

Capturing subtle details such as the sharp peak in k near the surface has been done at the expense of 10% differences between computed and measured velocity profiles for y^+ between 10 and 100, although the law of the wall is accurately predicted above $y^+ = 100$. This type of compromise is very typical of low-Reynolds-number versions of the LRR model as well. Unlike the multiscale model however, many low-Reynolds-number variants of the LRR model provide accurate descriptions of near-wall Reynolds stresses and dissipation while simultaneously giving nontrivial discrepancies between computed and measured skin friction. By contrast, the low-Reynolds-number corrections have virtually no effect on the multiscale model's predicted skin friction.

Interestingly, the multiscale model implements the LRR pressure-strain model for Π_{ij} without the pressure-echo correction. Hence, the strong effect this term has on LRR-model predictions may, to some extent, reflect shortcomings of the ϵ equation's near-wall behavior.

Rotating channel flow is an interesting application of second-order closure models. As with flow over a curved surface, two-equation models require ad hoc corrections for rotating channel flow in order to make realistic predictions [e.g., Launder, Priddin and Sharma (1977) and Wilcox and Chambers (1977)]. To understand the problem, note that in a rotating coordinate frame, the Coriolis acceleration yields additional inertial terms in the Reynolds-stress equation. Specifically, in a coordinate system rotating with angular velocity, Ω, the Reynolds-stress equation is

$$\frac{\partial \tau_{ij}}{\partial t} + U_k \frac{\partial \tau_{ij}}{\partial x_k} + 2\left(\epsilon_{jkm}\Omega_k\tau_{im} + \epsilon_{ikm}\Omega_k\tau_{jm}\right)$$
$$= -\tau_{ik}\frac{\partial U_j}{\partial x_k} - \tau_{jk}\frac{\partial U_i}{\partial x_k} + \epsilon_{ij} - \Pi_{ij} + \frac{\partial}{\partial x_k}\left[\nu\frac{\partial \tau_{ij}}{\partial x_k} + C_{ijk}\right] \quad (6.95)$$

where ϵ_{jkm} is the permutation tensor. Note that if the rotation tensor, Ω_{ij}, appears in any of the closure approximations for ϵ_{ij}, Π_{ij} or C_{ijk}, it must be replaced by $\Omega_{ij} + \epsilon_{ikj}\Omega_k$. Contracting Equation (6.95) yields the
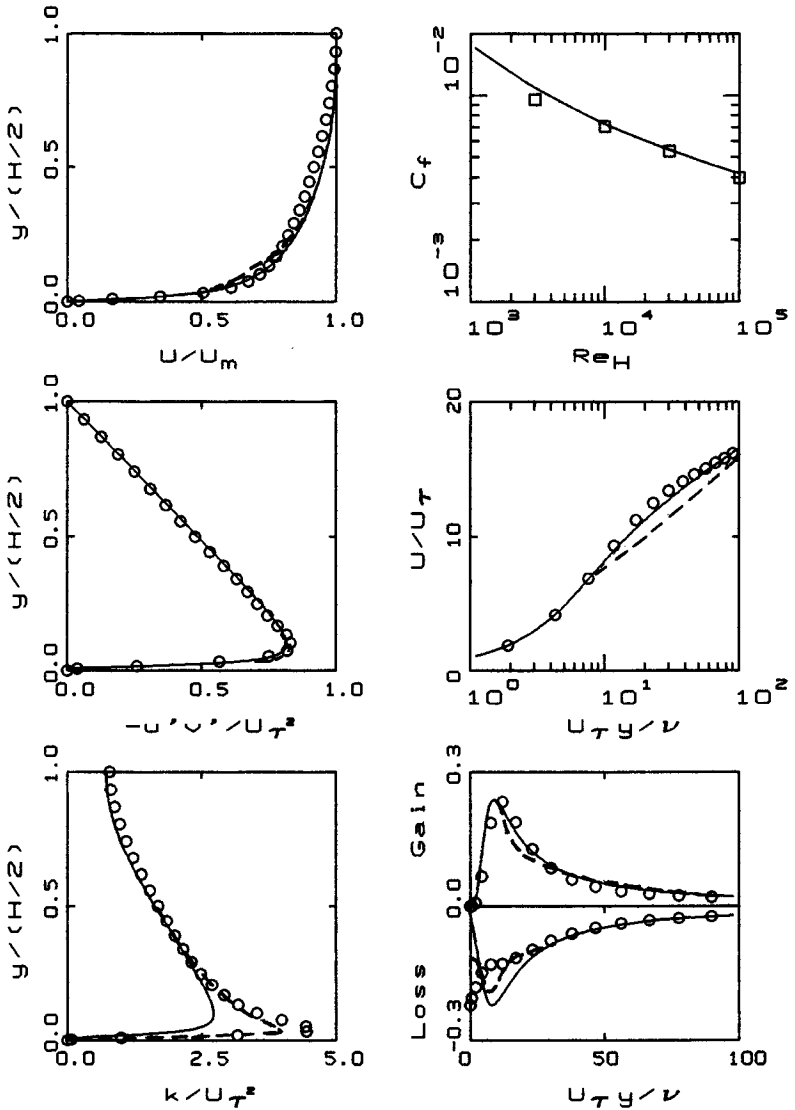
Figure 6.11: Comparison of computed and measured channel-flow properties, $Re_H = 13,750$. —— High-Reynolds-number multiscale model; - - - Low-Reynolds-number multiscale model; o Mansour et al. (DNS); □ Halleen-Johnston correlation.
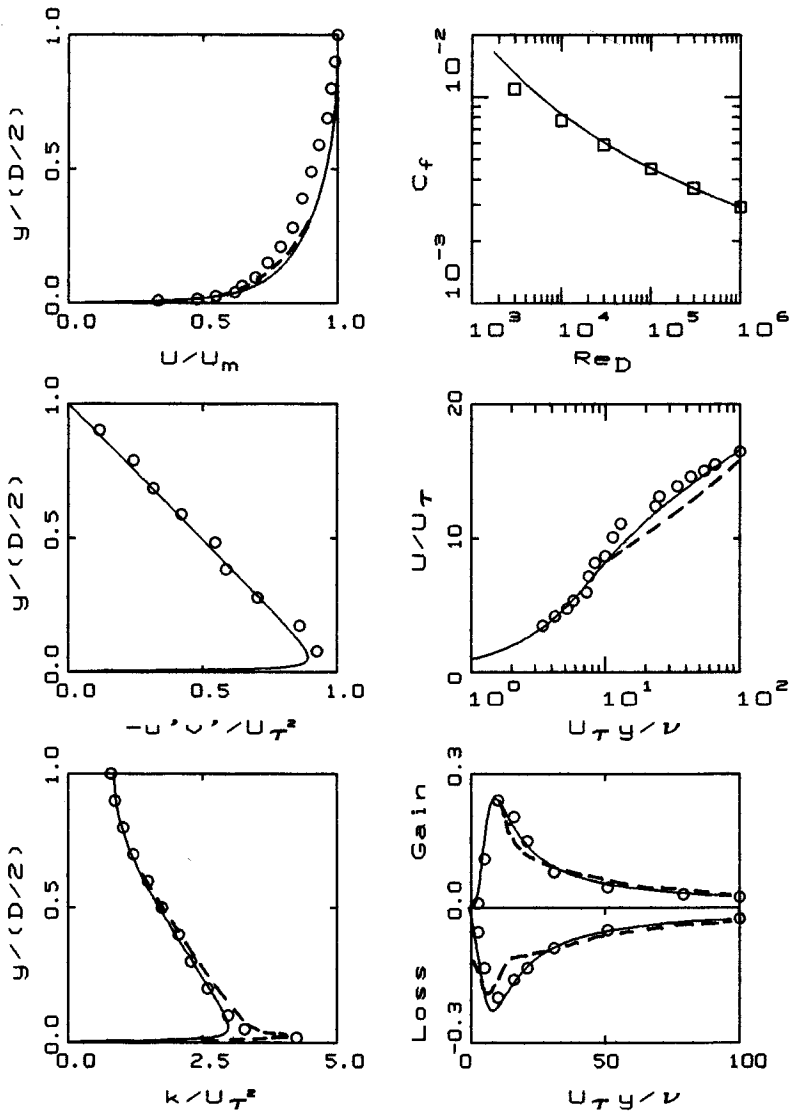
Figure 6.12: Comparison of computed and measured pipe-flow properties, $Re_D = 40,000$. —— High-Reynolds-number multiscale model; - - - Low-Reynolds-number multiscale model; o Laufer; □ Prandtl correlation.

turbulence kinetic energy equation. Because the trace of the Coriolis term is zero, there is no explicit effect of rotation appearing in the equation for k. Since rotation has a strong effect on turbulence, this shows why ad hoc modifications are needed for a two-equation model.

Figure 6.13 compares a computed and measured velocity profile for a channel with a constant angular velocity about the spanwise (z) direction. The computations have been done using the Gibson-Launder (1978) second-order closure model and the Standard k-ϵ model. The experimental data are those of Johnston et al. (1972), and correspond to an inverse Rossby number, $\Omega H/U_m = 0.21$, where H is the height of the channel and U_m is the average velocity. As shown, the k-ϵ model predicts a velocity profile that is symmetric about the center line. Consistent with measurements, the Gibson-Launder model predicts an asymmetric profile. However, as clearly shown in the figure, only qualitative agreement with measurements has been achieved.
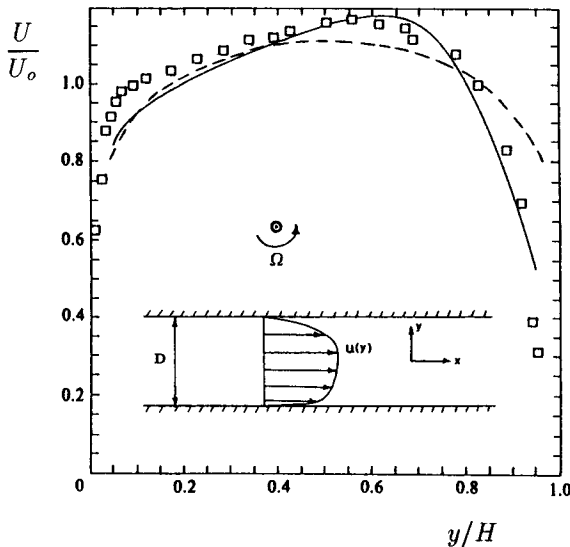

Figure 6.13: Computed and measured velocity profiles for rotating channel flow with $\Omega H/U_m = 0.21$; —— Gibson-Launder model; - - - k-ϵ model; □ Johnston et al. [From Speziale (1991) — Published with permission of author.]

6.6.3 Boundary Layers

Figure 6.14 compares computed and measured skin friction and velocity profiles for three incompressible boundary layers. The cases include the constant-pressure case [Coles and Hirst (1969) - Flow 1400], Bradshaw's adverse gradient case [Coles and Hirst (1969) - Flow 3300], and the Samuel-Joubert flow with increasingly adverse pressure gradient [Kline et al. (1981) - Flow 0141]. Computations have been done with the Wilcox (1988b) multiscale model for all three cases and with the Hanjalić-Launder (1980) low-Reynolds-number second-order closure model for Samuel-Joubert case.

Figures 6.14(a) and 6.14(b) compare computed and measured flat-plate boundary layer skin friction and velocity profiles for the multiscale model. As expected, differences between theory and experiment are almost insignificant, with the largest differences being less than 3%. Although not shown, most variants of the LRR model are as close to measurements as the multiscale model.

For the Bradshaw case, Figures 6.14(c) and 6.14(d) compare computed and measured skin friction and a velocity profile at the final station. Differences between theory and experiment are almost undetectable. For the Samuel-Joubert case, Figures 6.14(e) through 6.14(g) compare computed and measured flow properties. As shown, multiscale model skin friction differs from measured values by less than 3%, while the Hanjalić-Launder model's skin friction shows increasing differences approaching the final station. For both models, velocity profiles are nearly identical, and Reynolds shear stress profiles differ by less than 7% and 15% for the multiscale and Hanjalić-Launder models, respectively.

Centrifugal and Coriolis accelerations attending flow over curved surfaces have a significant effect upon structural features of the turbulent boundary layer. As discussed in Section 6.1, in the absence of ad hoc modifications, such effects cannot be accurately predicted with a two-equation model as curvature has a trivial effect on the turbulence kinetic energy equation. In principle, second-order closure models should display none of these shortcomings. Thus, computing curved-wall boundary layers poses an interesting test of second-order closure models.

Figure 6.15 presents results of two computations done with the Wilcox multiscale model for flow over a convex surface. The two cases are the constant-pressure and adverse-pressure-gradient flows that So and Mellor (1972) have investigated experimentally. To insure accurate starting conditions, the measured momentum and displacement thickness at $x = 2$ ft. have been matched to within 1% for both cases, a point well upstream of the beginning of the curved-wall portion of the flow at $x = 4.375$ ft. For both computations, computed and measured flow properties differ by less
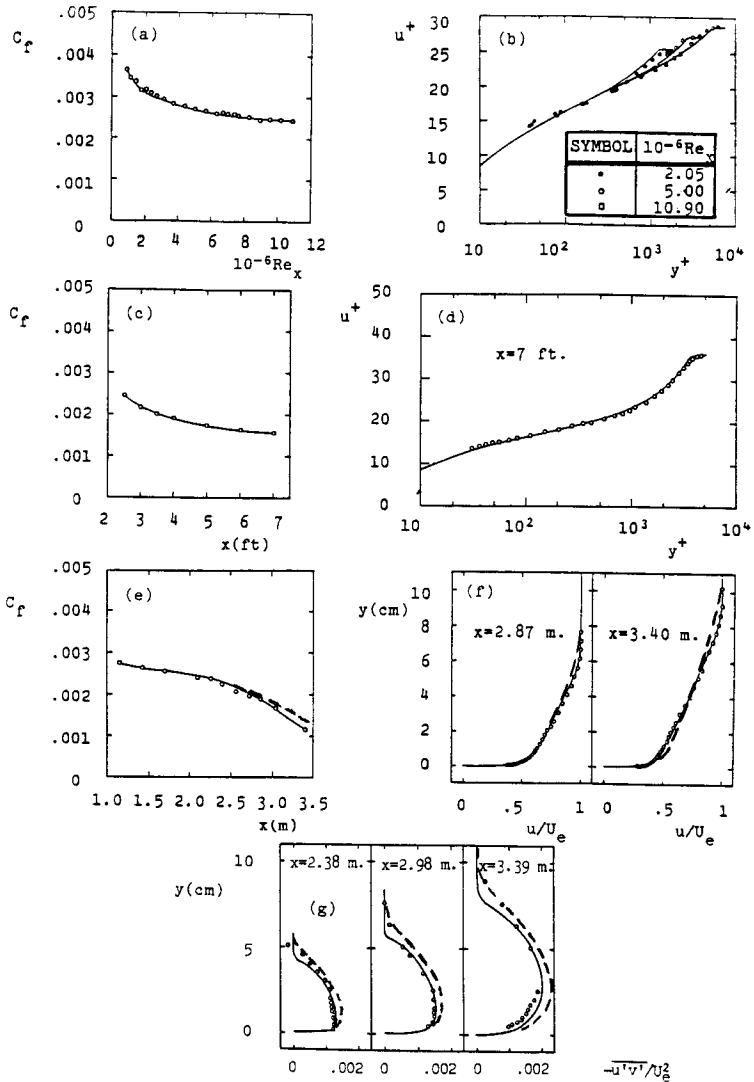
Figure 6.14: Comparison of computed and measured skin friction and pro-
files for incompressible boundary layers; —— Wilcox multiscale model;
- - - Hanjalić-Launder model; o ● □ Measured. [From Wilcox (1988b) —
Copyright © AIAA 1988 — Used with permission.]

than 6%. The LRR model also offers important improvement in predictive accuracy relative to the k-ϵ model for flows with curved streamlines. Lai et al. (1991), for example, have successfully applied three variants of the LRR model with wall functions to flow in a curved pipe. Consistent with measurements, their computations predict existence of secondary flows.

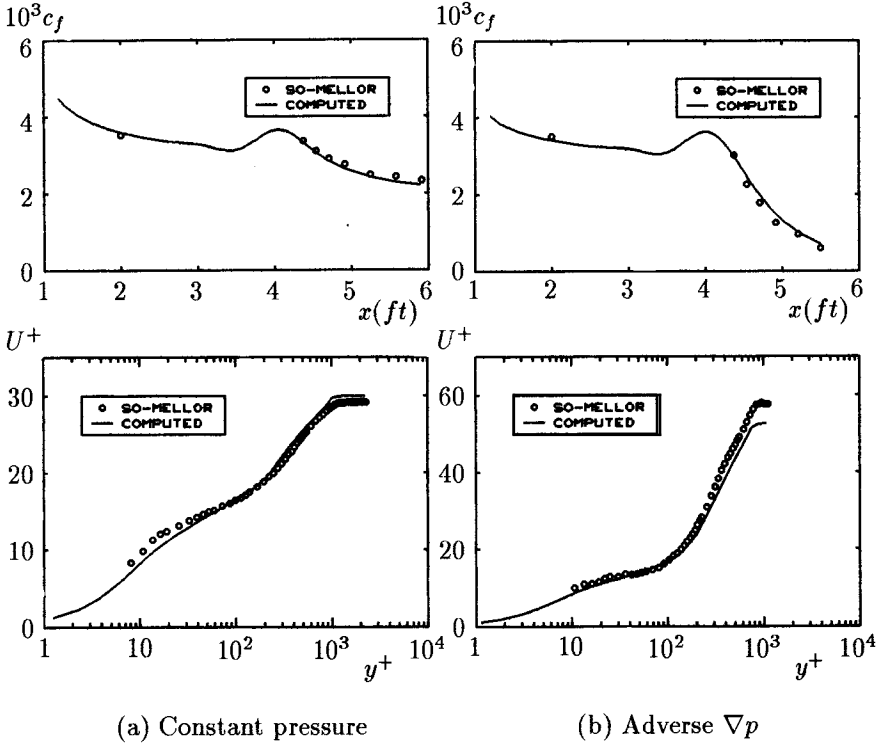(a) Constant pressure   (b) Adverse ∇p

Figure 6.15: Comparison of computed and measured skin friction for flow over a convex wall.

Turning to effects of compressibility, a second-order closure model's performance is intimately tied to the scale-determining equation. Models based on the ϵ equation will share the k-ϵ model's incorrect density scaling (see Section 5.6). By contrast, models based on the ω equation should share the k-ω model's ability to accurately predict the compressible law of the wall. Figure 6.16 confirms this point for the Wilcox multiscale model. The figure compares computed effects of Mach number and surface cooling on flat-plate boundary layer skin friction. Figure 6.16(a) compares computed

ratio of skin friction to the incompressible value, c_{f_o}, as a function of Mach number with the Van Driest correlation. Differences between computed ratios and correlated values are trivial. Figure 6.16(b) focuses upon effects of surface temperature on flat-plate skin friction at Mach 5. Differences between predicted values and correlated values nowhere exceed 4%.
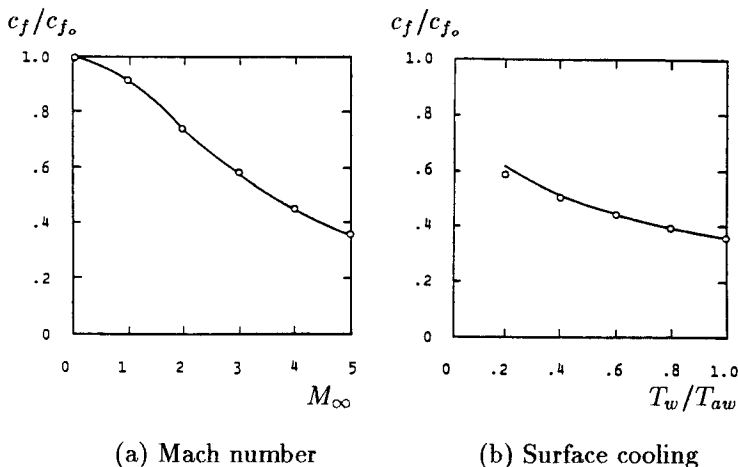

(a) Mach number   (b) Surface cooling

Figure 6.16: Comparison of computed and measured effect of freestream Mach number and surface cooling on flat-plate boundary-layer skin friction; —— Wilcox multiscale model; o Van Driest correlation. [From Wilcox (1988b) — Copyright © AIAA 1988 — Used with permission.]

Second-order closure models hold promise of more accurate predictions for flows in which the surface shear force is not parallel to the freestream velocity. Figure 6.17 compares computed and measured skin friction for such a flow, a boundary layer on a segmented cylinder, part of which rotates about its axis. The experiment was performed by Higuchi and Rubesin (1978). As shown, the Wilcox-Rubesin (1980) second-order closure model most accurately describes both the axial (c_{f_x}) and transverse (c_{f_z}) skin friction components in the relaxation zone i.e., the region downstream of the spinning segment. The Cebeci-Smith algebraic model and the Wilcox-Rubesin (1980) two-equation model yield skin friction components that differ from measured values by as much as 20% and 10%, respectively.

The final round of applications is for incompressible, unsteady turbulent boundary layers. These flows pose a difficult challenge to a turbulence model because many complicated frequency-dependent phenomena are generally present, including periodic separation and reattachment.
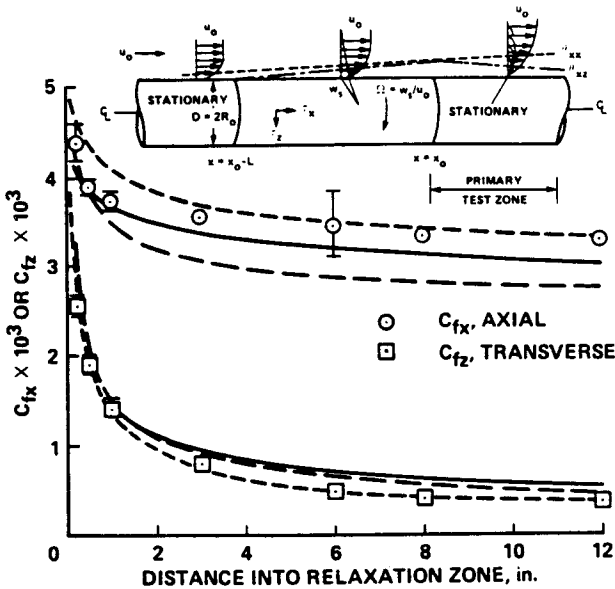
Figure 6.17: Skin friction on a segmented spinning cylinder; —— Cebeci-Smith model; — — Wilcox-Rubesin k-ω^2 model; - - - Wilcox-Rubesin second-order closure model; ○□ Higuchi and Rubesin. [From Rubesin (1989) — Copyright ©AIAA — Used with permission.]

Wilcox (1988b) has simulated the experiments performed by Jayaraman, Parikh and Reynolds (1982). In these experiments, a well developed steady turbulent boundary layer enters a test section which has been designed to have freestream velocity that varies according to:

$$U_e = U_o \left\{ 1 - ax'[1 - cos(2\pi ft)] \right\}, \quad x' = (x - x_0)/(x_1 - x_0) \quad (6.96)$$

The quantity x' is fractional distance through the test section where x_0 and x_1 are the values of streamwise distance, x, at the beginning and end of the test section, respectively. Thus, an initially steady turbulent boundary layer is subjected to a sinusoidally varying adverse pressure gradient. The experiments were performed for low- and high-amplitude unsteadiness characterized by having $a \approx 0.05$ and 0.25, respectively. For both amplitudes, experiments were conducted for five frequencies, f, ranging from 0.1 Hz to 2.0 Hz. Wilcox simulates nine of the experiments, including all of the low-amplitude cases and all four of the high-amplitude cases.

In order to compare computed and measured flow properties, we must decompose any flow property $y(\mathbf{x}, t)$ in terms of three components, viz.,

$$y(\mathbf{x}, t) = \bar{y}(\mathbf{x}) + \tilde{y}(\mathbf{x}, t) + y'(\mathbf{x}, t) \qquad (6.97)$$

where $\bar{y}(\mathbf{x})$ is the long-time averaged value of $y(\mathbf{x}, t)$, $\tilde{y}(\mathbf{x}, t)$ is the organized response component due to the imposed unsteadiness, and $y'(\mathbf{x}, t)$ is the turbulent fluctuation. Using an unsteady boundary layer program, Wilcox computes the phase averaged component, $< y(\mathbf{x}, t) >$, defined by

$$< y(\mathbf{x}, t) >= \bar{y}(\mathbf{x}) + \tilde{y}(\mathbf{x}, t) \qquad (6.98)$$

Jayaraman et al. expand $< y(\mathbf{x}, t) >$ in a Fourier series according to

$$< y(\mathbf{x}, t) >= \bar{y}(\mathbf{x}) + \sum_{n=1}^{\infty} A_{n,y}(\mathbf{x}) \cos\left[2n\pi ft + \phi_{n,y}(\mathbf{x})\right] \qquad (6.99)$$

Velocity profile data, for example, are presented by Jayaraman et al. in terms of $\bar{u}(\mathbf{x})$, $A_{1,u}(\mathbf{x})$ and $\phi_{1,u}(\mathbf{x})$. These quantities can be extracted from the boundary-layer solution by the normal Fourier decomposition, viz., by computing the following integrals.

$$\bar{u}(\mathbf{x}) = f \int_{0}^{1/f} < u(\mathbf{x}, t) > dt \qquad (6.100)$$

$$A_{1,u}(\mathbf{x}) \cos\phi_{1,u} = f \int_{0}^{1/f} < u(\mathbf{x}, t) > \cos\left(2\pi ft\right) dt \qquad (6.101)$$

$$A_{1,u}(\mathbf{x}) \sin\phi_{1,u} = -f \int_{0}^{1/f} < u(\mathbf{x}, t) > \sin\left(2\pi ft\right) dt \qquad (6.102)$$

Figure 6.18 compares the computed and measured velocity profiles at $x' = 0.88$ for the five low-amplitude cases. As shown, computed mean velocity profiles differ from corresponding measured profiles by no more than 5% of scale. Comparison of computed and measured $A_{1,u}$ profiles shows that, consistent with measurements, unsteady effects are confined to the near-wall Stokes layer at the higher frequencies ($f > .5$ Hz). By contrast, at the two lowest frequencies, the entire boundary layer is affected with significant amplification of the organized component occurring away from the surface. Differences between the numerical and experimental $A_{1,u}$ profiles are less than 10%. Computed and measured phase, $\phi_{1,u}$, profiles are very similar with differences nowhere exceeding 5°.
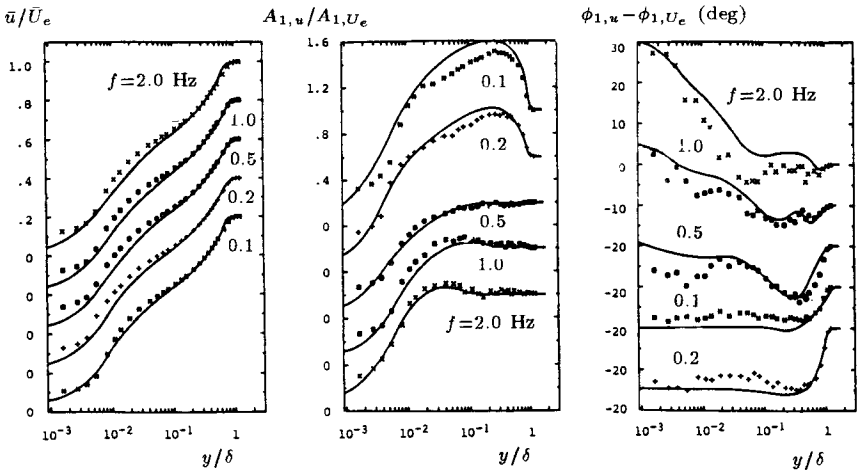
Figure 6.18: Comparison of computed and measured mean velocity, $A_{1,u}$ and phase profiles at $x' = 0.88$ for low amplitude; ——— multiscale model; ● Jayaraman, et al. [From Wilcox (1988b) — Copyright © AIAA 1988 — Used with permission.]

Figure 6.19 compares the computed and measured velocity profiles at $x' = 0.94$ for the high-amplitude cases. As for low amplitude, computed and measured $\bar{u}(\mathbf{x})$ profiles lie within 5% of scale of each other. Similarly, computed $A_{1,u}$ and $\phi_{1,u}$ profiles differ from corresponding measurements by less than 10%. To provide a measure of how accurately temporal variations have been predicted, Figure 6.20 compares computed and measured shape factor through a complete cycle for all four frequencies. Differences between computed and measured shape factors are less than 5%.

The four high-amplitude cases have also been computed using the Standard k-ω model. Results are included in Figure 6.20, which shows that k-ω and multiscale-model predictions differ by only a few percent. Although it is possible the test cases are not as difficult as might be expected, this seems unlikely in view of the wide Strouhal number range and the fact that periodic separation and reattachment are present. More likely, the k-ω model fares well because all of the cases have attached boundary layers through most of each cycle and in the mean.

As a closing comment, many recent turbulence modeling efforts focusing on unsteady boundary layers mistakenly credit their success (or lack of it) to achieving asymptotic consistency with the k-ϵ model or with second-order closure models based on the ϵ equation. The computations described
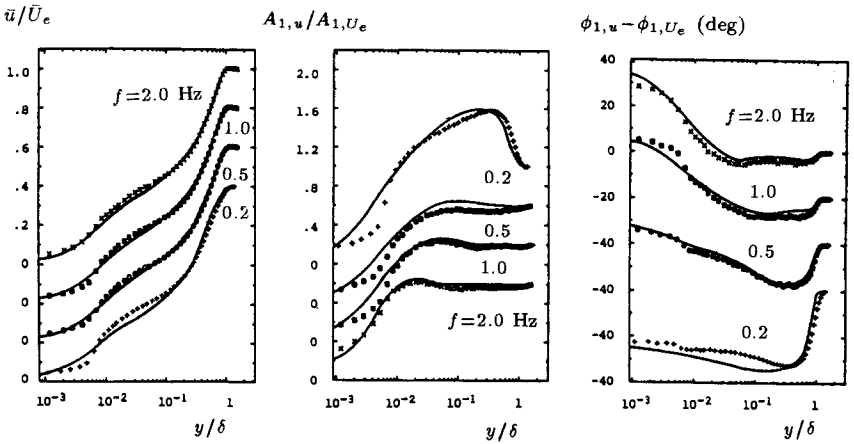
Figure 6.19: Comparison of computed and measured mean velocity, $A_{1,u}$ and phase profiles at $x' = 0.94$ for high amplitude; —— multiscale model; • Jayaraman, et al. [From Wilcox (1988b) — Copyright © AIAA 1988 — Used with permission.]
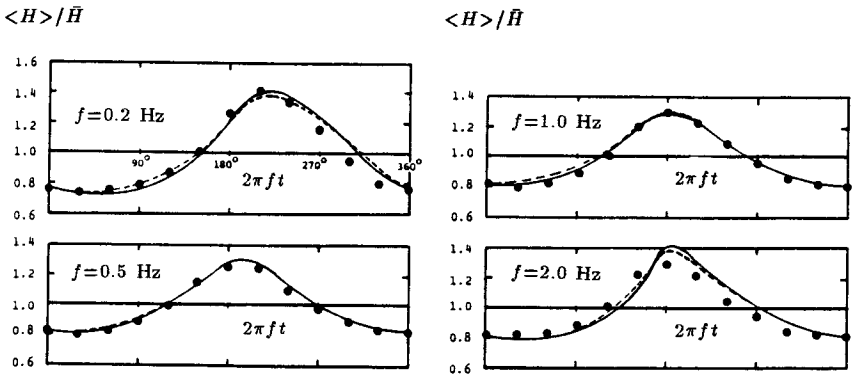

Figure 6.20: Comparison of computed and measured temporal variation of shape factor for the high-amplitude cases; - - - k-ω model; —— multiscale model; • Jayaraman, et al. [From Wilcox (1988b) — Copyright © AIAA 1988 — Used with permission.]

above were done using the high-Reynolds-number versions of the k-ω and multiscale models, neither of which is asymptotically consistent. All that appears to be necessary is to achieve a satisfactory value for the constant, B, in the law of the wall. This makes sense physically as the dissipation time scale is so short in the sublayer that the sublayer responds to changes in the mean flow almost instantaneously and thus behaves as a quasi-steady region. Consequently, achieving asymptotically consistent behavior in the sublayer is neither more nor less important for unsteady flows than it is for steady flows.

6.7 Application to Separated Flows

As we have seen in preceding chapters, turbulence models that use the Boussinesq approximation generally are unreliable for separated flows, especially shock-induced separation. Figure 5.8, for example, illustrates how poorly such models perform for Mach 3 flow into a compression corner. The figure also shows the surface pressure computed with the Wilcox (1988b) multiscale model, and it lies much closer to measured values than any of the algebraic and two-equation models. In this section, we will take a close look at how well second-order closure models perform for several separated flows.

Because second-order closure models require more computer resources than algebraic and two-equation models, applications to such flows have not been made until recently. Consequently, only preliminary conclusions can be drawn from the limited work that has been done at present. Incompressible applications have generally been limited to the backward-facing step, while compressible-flow applications have been done for compression corners for a limited range of Mach numbers.

Focusing first on the backward-facing step, So et al. (1988) have done an interesting study using a variety of closure approximations. Their computations use Chien's (1982) low-Reynolds number version of the ϵ equation. Most importantly, they have used three different models for the pressure-strain correlation, viz., the models of Rotta (1951) [Model A1], Launder, Reece and Rodi (1975) [Model A2], and Gibson and Younis (1986) [Model A4]. Using the Rotta model, computations have been done with wall functions as well [Model H-A1]. For reference, their computations also include the Chien (1982) low-Reynolds-number k-ϵ model [Model Lk-ϵ]. These models differ mainly in their representation of the fast pressure-strain term, with the Rotta model ignoring it altogether. The computations simulate the experiments of Eaton and Johnston (1980), for which the measured reattachment length is 8 step heights.
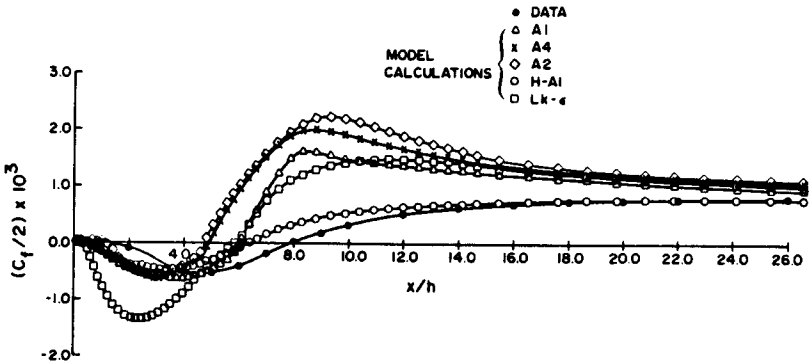
Figure 6.21: Computed and measured skin friction for flow past a backward-facing step; A1=Rotta model; A2=LRR model; A4=Gibson-Younis model; H-A1=Rotta model with wall functions; Lk-ϵ=Chien k-ϵ model; •=Eaton and Johnston. [From So et al. (1988) — Published with permission.]

As shown in Figure 6.21, computed reattachment length for all of their computations lies between 5 and 6 step heights, so that their result closest to measurements differs from the measured value by 25%. All of the models show large discrepancies between computed and measured wall pressure, while peak skin friction values are as much as 3 times measured values downstream of reattachment for the low-Reynolds-number models. In general, the second-order closure model skin friction results are as far from measurements as those of the low-Reynolds-number k-ϵ model. Only when wall functions are used with the second-order closure model does the computed skin friction lie reasonably close to measured values. So et al. note that the smallest discrepancies between computed and measured flow properties are obtained with the Rotta pressure-strain model, which omits the rapid pressure-strain correlation. That is, the LRR and Gibson-Younis models for the rapid pressure strain appear to yield larger discrepancies between computed and measured values.

Recalling how close to measurements k-ω model predictions are for flow past a backward-facing step (Section 4.10), the So et al. computations strongly suggest that their poor predictions are caused by use of the ϵ equation. On the one hand, comparison of Figures 4.29 and 6.21 show that for second-order closure model H-A1, c_f is very similar to k-ϵ model c_f when wall functions are used. Although the flows are a little different, in both cases the reattachment length is 25% smaller than measured. On the other

hand, using the same low-Reynolds-number ϵ equation, c_f for second-order closure model A1 is very similar to the low-Reynolds-number k-ϵ model c_f, except in the reverse flow region. Despite the latter difference, the reattachment length is the same in this case also. Thus, as with two-equation models, a second-order closure model's performance for the backward-facing step is intimately linked to the scale-determining equation. This strongly suggests that much closer agreement between computed and measured flow properties would be obtained with a second-order closure model based on the ω equation, such as the Wilcox multiscale model. Unfortunately, the multiscale model has not been applied to the backward-facing step, so this must remain a point of conjecture until such a computation is done.

Turning to compressible flows, Wilcox (1990) has done a numerical study that provides a definitive measure of differences attending use of the multiscale model compared to the k-ω model. The study includes results of three shock-separated turbulent boundary-layer computations using both the multiscale and k-ω models. The flows considered include two planar compression-corner flows and an axisymmetric compression-corner flow.

The first of the three applications is for Mach 2.79 flow into a 20° compression corner. This flow has been experimentally investigated by Settles, Vas and Bogdonoff (1976) and includes a small region over which separation of the incident turbulent boundary layer occurs. Figure 6.22(a) compares computed and measured surface pressure, p_w/p_∞, and skin friction, c_f. The multiscale model predicts more upstream influence, a lower pressure plateau at separation, and a more gradual increase in skin friction downstream of reattachment relative to the k-ω results. All of these features represent significant improvement in predictive accuracy. Using the k-ϵ model and specially devised wall functions, Viegas, Rubesin and Horstman (1985) are able to achieve similar accuracy for this flow.

The second of the three applications is for Mach 2.84 flow into a 24° compression corner. This flow has also been experimentally investigated by Settles, Vas and Bogdonoff (1976) and includes a larger region over which separation of the incident turbulent boundary layer occurs than in the 20° case of the preceding section. Figure 6.22(b) compares computed and measured surface pressure and skin friction. As in the 20° compression-corner computation, the multiscale model predicts much more upstream influence. Interestingly, the k-ω predicted pressure plateau at separation is very close to the measured level, and there is little difference between k-ω and multiscale predicted increase in skin friction downstream of reattachment. Note that, for this flow, Viegas, Rubesin and Horstman (1985) predict pressure plateau values about 20% higher than measured, and are unable to simultaneously make accurate predictions for skin friction downstream of reattachment and the initial rise in surface pressure. That is, their solutions

can match either skin friction or surface pressure, but not both.

The third application is for Mach 2.85 flow into a 30° axisymmetric compression corner. This flow has been experimentally investigated by Brown (1986) and includes a separation bubble of length comparable to the 24° planar compression corner. Figure 6.22(c) compares computed and measured surface pressure. Computed skin friction is also shown. Once again the multiscale model predicts much more upstream influence. For both models, the predicted pressure plateau at separation is about 10% higher the measured level, and there is little difference between k-ω and multiscale predicted increase in skin friction downstream of reattachment. The overall pressure rise is predicted by both models to be 4.7, while the measurements indicate a value of 4.0. The inviscid pressure rise for a 30° axisymmetric compression corner is 4.4, so that neither theory nor experiment appears to be completely consistent with the physics of this flow.

Clearly, for the three compression-corner cases considered, the multiscale model provides a flowfield more consistent with experimental observations than does the k-ω model. The primary reason for the difference in the two models' predictions can be found by examining predicted behavior of the Reynolds shear stress near the separation point. Figure 6.22(d) shows the maximum Reynolds shear stress, τ_{max}, throughout the interaction region for the three compression-corner computations. As shown, the k-ω model predicts a more abrupt increase in τ_{max} at separation and a much larger peak value than predicted by the multiscale model. For the axisymmetric case, the figure includes experimental data for points ahead of the measured separation point. As shown, the multiscale-model predicted τ_{max} falls within experimental data scatter.

The physical implication of the pronounced difference in the rate of amplification of the Reynolds shear stress is clear. Using the Boussinesq approximation, the k-ω model makes a far more rapid adjustment to the rotation of the mean strain rate tensor's principal axes than the multiscale model. Consequently, the predicted separation point and initial pressure rise lie closer to the corner with the k-ω model than measured. Predicting more physically realistic growth of the Reynolds stresses, the multiscale model predicts overall flow properties which are in much closer agreement with measurements.

It is interesting to note that for the multiscale model, although the pressure is in such close agreement with measurements, the numerical separation points are further upstream than indicated by oil flow measurements for all three compression corner cases. Marshall and Dolling (1992) indicate that these flows include a low-frequency oscillation of the separation shock. The time-mean pressure distribution upstream of the corner is affected by these oscillations whose frequency content includes substantial energy at time
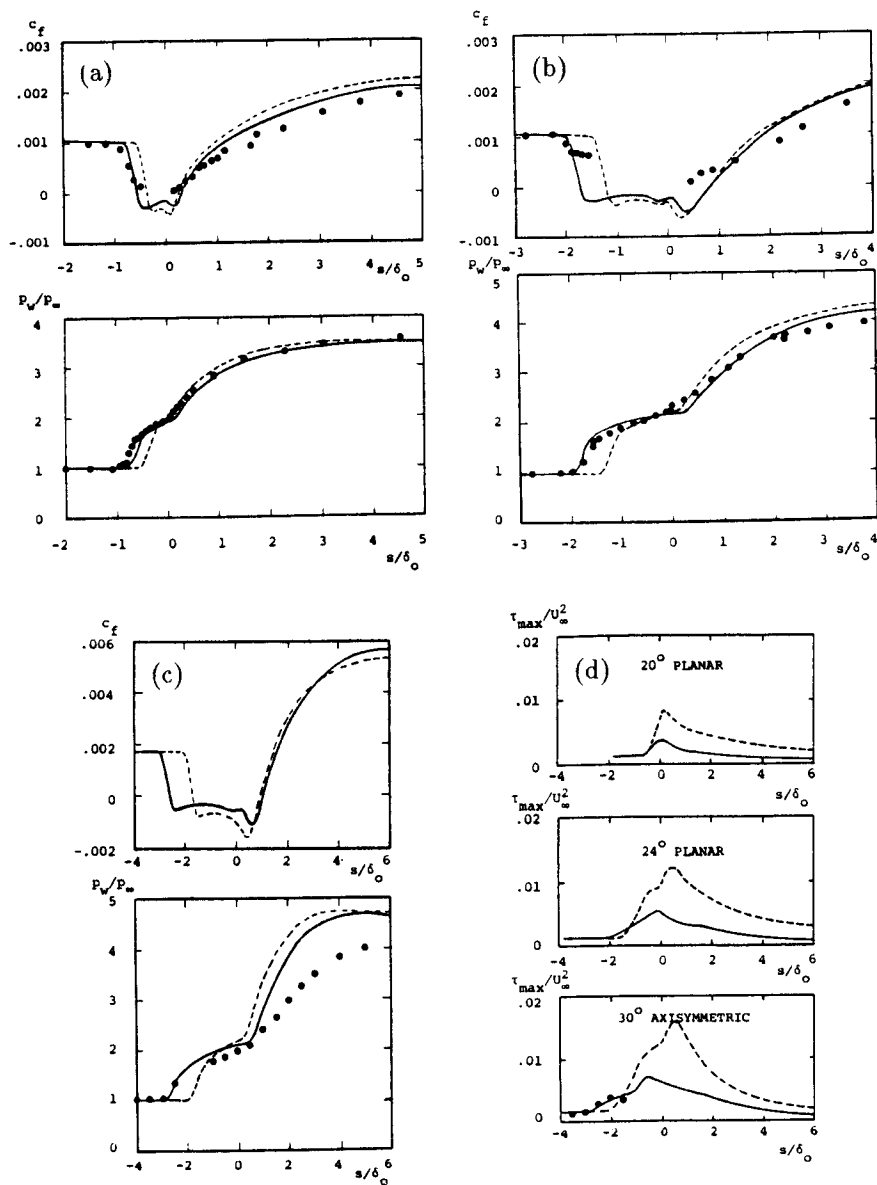
Figure 6.22: Computed and measured properties for supersonic compression corners; s is tangential distance from corner; - - - k-ω model; —— multiscale model; (a) and (b) ● Settles et al.; (c) and (d) ● Brown. [From Wilcox (1990) — Copyright © AIAA 1990 — Used with permission.]

scales of the mean motion. This unsteadiness is responsible for the apparent mismatch between the beginning of the pressure rise and the separation point. Since computations with the multiscale model and the k-ω model fail to display any low-frequency oscillation of the shock, more research is needed to arrive at a completely satisfactory solution.

6.8 Range of Applicability

The two primary approaches to removing the limitations of the Boussinesq approximation are to use either a **nonlinear constitutive relation** or a **second-order closure model**. As discussed in Section 6.2, nonlinear constitutive relations offer some advantage over the Boussinesq approximation, most notably for flows in which anisotropy of the normal Reynolds stresses is important. **Algebraic Stress Models** provide a straightforward method for accurately predicting effects of streamline curvature and system rotation, although ad hoc corrections to standard two-equation models are just as effective. However, nonlinear constitutive relations offer no improvement over the Boussinesq approximation for flows with sudden changes in mean strain rate.

Despite their complexity, second-order closure models have great potential for removing shortcomings of the Boussinesq approximation in a natural way. Without ad hoc corrections, second-order closure models provide physically realistic predictions for flows with curved streamlines, system rotation, stratification, sudden changes in mean strain rate, secondary motions, and anisotropic shear. While more research is needed for separated flows, these models may also improve predictions for shock-separated flows. However, to be completely objective in our assessment, we must also note that in many such applications only qualitative agreement between theory and experiment has been obtained.

Just as one-equation turbulence models share the shortcomings and successes of the mixing-length model, second-order closure models reflect the strengths and weaknesses of the scale-determining equation used with the model. There is an increasing pool of evidence that many of the shortcomings of second-order closure models are caused by the scale-determining equation. Results obtained for the Samuel-Joubert boundary layer (Subsection 6.6.3) and the backward-facing step (Section 6.7) strongly suggest that predictions of standard second-order closure models can be improved by using the ω equation in place of the ϵ equation.

From a numerical point of view, second-order closure models are at least as difficult to solve as the corresponding two-equation model. Models based on the ϵ equation fail to predict a satisfactory law of the wall and require

complicated viscous damping functions. Correspondingly, such models are generally very difficult to integrate. By contrast, models based on the ω equation require no special viscous corrections, and are much easier to integrate. In particular, the Wilcox multiscale model usually requires about 25% to 40% more computing time relative to corresponding two-equation models. Hence, the scale-determining equation may be even more important for second-order closure models than for two-equation models.

Problems

6.1 The objective of this problem is to derive the modified law of the wall for flow over a curved wall according to the k-ω model.

(a) Verify that the dimensionless form of Equations (6.3) to (6.5) in the log layer is [with $\epsilon \equiv \nu/(u_\tau \mathcal{R})$]:

$$\nu_T^+ \left(\frac{\partial U^+}{\partial y^+} - \epsilon U^+ \right) = 1, \qquad \nu_T^+ = \frac{k^+}{\omega^+}$$

$$\sigma^* \nu_T^+ \frac{\partial}{\partial y^+} \left[\nu_T^+ \frac{\partial k^+}{\partial y^+} \right] = \beta^* (k^+)^2 - 1 + \frac{9}{2} \epsilon (\nu_T^+)^2 U^+ \frac{\partial U^+}{\partial y^+}$$

$$\sigma \nu_T^+ \frac{\partial}{\partial y^+} \left[\nu_T^+ \frac{\partial \omega^+}{\partial y^+} \right] = \beta k^+ \omega^+ - \alpha \frac{\omega^+}{k^+}$$

(b) Assume a solution of the form

$$\frac{dU^+}{dy^+} \sim \frac{1}{\kappa y^+} \left[1 + \epsilon a y^+ \ell n y^+ + O(\epsilon^2) \right]$$

$$k^+ \sim \frac{1}{\sqrt{\beta^*}} \left[1 + \epsilon b y^+ \ell n y^+ + O(\epsilon^2) \right]$$

$$\omega^+ \sim \frac{1}{\sqrt{\beta^*} \kappa y^+} \left[1 + \epsilon c y^+ \ell n y^+ + O(\epsilon^2) \right]$$

with $\epsilon \ll 1$. Substitute into the equations for k^+ and ω^+ and verify that the coefficients b and c are given by

$$b = -\frac{9/2}{2 - \sigma^* \kappa^2 / \sqrt{\beta^*}} \qquad \text{and} \qquad c = \frac{\alpha}{\alpha - \beta/\beta^*} b$$

NOTE: Use the fact that the k-ω model closure coefficients are related by $\sigma \kappa^2 = (\beta/\beta^* - \alpha)\sqrt{\beta^*}$ and ignore terms proportional to y^+ relative to terms proportional to $y^+ \ell n y^+$.

(c) Substitute into the momentum equation and verify that

$$a + b - c = 1$$

(d) Using $\alpha = 5/9$, $\beta = 3/40$, $\beta^* = 9/100$, $\sigma = 1/2$ and $\sigma^* = 1/2$, determine the numerical values of a, b and c, and show that the modified law of the wall is of the form

$$\left[1 - \beta_R \frac{y}{\mathcal{R}} \right] \frac{U}{u_\tau} \sim \frac{1}{\kappa} \ell n \left(\frac{u_\tau y}{\nu} \right) + \cdots$$

where $\beta_R \approx 8.8$.

6.2 For incompressible flow, we wish to use Speziale's non-linear constitutive relation with the k-ω model. In terms of k-ω model parameters, the relation can be written as

$$\tau_{ij} = -\frac{2}{3}\rho k\delta_{ij} + 2\mu_T S_{ij} + C_D \frac{\rho k}{\beta^*\omega^2}\left(S_{ik}S_{kj} - \frac{1}{3}S_{mn}S_{nm}\delta_{ij}\right)$$
$$+C_E \frac{\rho k}{\beta^*\omega^2}\left(\overset{\circ}{S}_{ij} - \frac{1}{3}\overset{\circ}{S}_{mm}\delta_{ij}\right)$$

where C_D and C_E are closure coefficients whose values are to be determined.

(a) Verify for incompressible boundary layers that

$$S_{xy} = S_{yx} = \frac{1}{2}\frac{\partial U}{\partial y}; \qquad \text{all other } S_{ij} \approx 0$$

$$\overset{\circ}{S}_{xx} = -\left(\frac{\partial U}{\partial y}\right)^2; \qquad \text{all other } \overset{\circ}{S}_{ij} \approx 0$$

(b) Express the Reynolds-stress components τ_{xy}, τ_{xx}, τ_{yy} and τ_{zz} in terms of ρ, k, μ_T, β^*, ω and $\partial U/\partial y$ for incompressible boundary layers.

(c) Using the stresses derived in part (b), write the log-layer form of the mean-momentum, k and ω equations.

(d) Assuming a solution of the form $\partial U/\partial y = u_\tau/(\kappa y)$ and $k = $ constant, verify that

$$\left(\frac{\partial U}{\partial y}\right)^2 = \beta^*\omega^2$$

(e) Verify that

$$\overline{u'^2}/k = (8 - C_D + 8C_E)/12$$

$$\overline{v'^2}/k = (8 - C_D - 4C_E)/12$$

$$\overline{w'^2}/k = (8 + 2C_D - 4C_E)/12$$

(f) Determine the values of C_D and C_E that are consistent with the normal Reynolds stresses standing in the ratio

$$\overline{u'^2} : \overline{v'^2} : \overline{w'^2} = 4 : 2 : 3$$

6.3 Verify that in the log layer of an incompressible flat-plate boundary layer, the Wilcox-Rubesin nonlinear constitutive relation [Equation (6.13)] predicts that the normal Reynolds stresses stand in the ratio

$$\overline{u'^2} : \overline{v'^2} : \overline{w'^2} = 4 : 2 : 3$$

HINT: Recall that in the log layer, $\partial U/\partial y \approx \sqrt{\beta^*}\, \omega$.

6.4 For incompressible flow in a rectangular duct, the strain rate and rotation tensors are approximately

$$S_{ij} = \begin{bmatrix} 0 & \frac{1}{2}\frac{\partial U}{\partial y} & \frac{1}{2}\frac{\partial U}{\partial z} \\ \frac{1}{2}\frac{\partial U}{\partial y} & 0 & 0 \\ \frac{1}{2}\frac{\partial U}{\partial x} & 0 & 0 \end{bmatrix} \quad \text{and} \quad \Omega_{ij} = \begin{bmatrix} 0 & \frac{1}{2}\frac{\partial U}{\partial y} & \frac{1}{2}\frac{\partial U}{\partial z} \\ -\frac{1}{2}\frac{\partial U}{\partial y} & 0 & 0 \\ -\frac{1}{2}\frac{\partial U}{\partial x} & 0 & 0 \end{bmatrix}$$

Determine τ_{xy}, τ_{xz}, τ_{yz} and $(\tau_{zz} - \tau_{yy})$ according to the Wilcox-Rubesin nonlinear constitutive relation [Equation (6.13)].

6.5 Derive the Poisson equation [Equation(6.38)] for the fluctuating pressure.

6.6 Consider the Launder-Reece-Rodi (LRR) rapid pressure strain closure approximation, Equation (6.50).

(a) Verify that a_{ijkl} satisfies the symmetry constraints in Equation (6.48).

(b) Invoke the constraints of Equation (6.49) and verify that α, β, η and υ are given by Equation (6.51).

(c) Form the tensor product

$$M_{ijkl}\frac{\partial U_k}{\partial x_l} = (a_{ijkl} + a_{jikl})\frac{\partial U_k}{\partial x_l}$$

and verify Equations (6.52) through (6.54).

6.7 Consider Lumley's general representation for Π_{ij} in Equation (6.56). Show that the LRR pressure-strain model [including A_{ij} as defined in Equation (6.45)] is the limiting case where all coefficients other than a_0, a_2, a_7 and a_9 equal to zero. Also, assuming $C_1 = 1.8$, determine the values of a_0, a_2, a_7 and a_9 that correspond to $C_2 = 0.4$, 0.5 and 0.6. Assume the flow is incompressible.

6.8 Consider the Launder, Reece and Rodi second-order closure model, Equations (6.60) - (6.64). This problem analyzes the model's predicted asymptotic solution for homogeneous plane shear, in which

$$
\frac{\partial U_i}{\partial x_j} = \begin{bmatrix} 0 & S & 0 \\ 0 & 0 & 0 \\ 0 & 0 & 0 \end{bmatrix}
$$

(a) Assuming that $\epsilon/k \rightarrow$ constant as $t \rightarrow \infty$, verify that

$$
\frac{P}{\rho\epsilon} \rightarrow \frac{C_{\epsilon 2} - 1}{C_{\epsilon 1} - 1}
$$

where $P = S\tau_{xy}$.

(b) Neglecting the pressure-echo effect, verify that

$$
P_{ij} = \begin{bmatrix} 2S\tau_{xy} & S\tau_{yy} & S\tau_{yz} \\ S\tau_{yy} & 0 & 0 \\ S\tau_{yz} & 0 & 0 \end{bmatrix}, \quad D_{ij} = \begin{bmatrix} 0 & S\tau_{xx} & 0 \\ S\tau_{xx} & 2S\tau_{xy} & S\tau_{xz} \\ 0 & S\tau_{xz} & 0 \end{bmatrix}
$$

(c) Assuming a solution of the form $\tau_{ij} = C_{ij} e^{\lambda t}$ where C_{ij} is independent of time and λ is a constant, verify that if τ_{xz} and τ_{yz} are initially zero, they are always zero, provided $\hat{\beta}(1 - \hat{\alpha}) > 0$.

(d) Determine ϵ/k and $P/(\rho k)$ as functions of $C_{\epsilon 1}$, $C_{\epsilon 2}$ and λ under the assumption that $\tau_{ij} = C_{ij} e^{\lambda t}$.

(e) Using results of Parts (a) - (d), determine $\overline{u'^2}/k$, $\overline{v'^2}/k$ and $\overline{w'^2}/k$ as algebraic functions of the closure coefficients. **HINT:** You can simplify your computations somewhat by first writing the equation for τ_{ij} as an equation for $\tau_{ij} + \frac{2}{3}\rho k \delta_{ij}$.

(f) Using the following two sets of closure coefficient values, compute the numerical values of $\overline{u'^2}/k$, $\overline{v'^2}/k$ and $\overline{w'^2}/k$.

   1. Original LRR: $C_1 = 1.5$, $C_2 = 0.4$, $C_{\epsilon 1} = 1.44$, $C_{\epsilon 2} = 1.90$
   2. Revised LRR: $C_1 = 1.8$, $C_2 = 0.6$, $C_{\epsilon 1} = 1.44$, $C_{\epsilon 2} = 1.92$

6.9 Consider the Launder, Reece and Rodi second-order closure model, Equations (6.60) - (6.64).

(a) State the limiting form of the equations for the incompressible, two-dimensional log layer.

(b) Assuming a solution of the form

$$\frac{dU}{dy} \sim \frac{u_\tau}{\kappa y}, \qquad k \sim \frac{u_\tau^2}{\sqrt{C_\mu}}, \qquad \epsilon \sim \frac{u_\tau^3}{\kappa y}$$

determine κ, $-\overline{u'v'}/k$, $\overline{u'^2}/k$, $\overline{v'^2}/k$ and $\overline{w'^2}/k$ as algebraic functions of the closure coefficients. **HINTS:** All are constant. Also, the ϵ equation yields κ as a function of the closure coefficients and $\overline{v'^2}/k$. You needn't simplify further.

(c) Using the closure coefficient values in Equation (6.64), verify that $\kappa \approx 0.39$, $-\overline{u'v'}/k \approx 0.36$, and $\overline{u'^2} : \overline{v'^2} : \overline{w'^2} \approx 4 : 2.2 : 3.2$. **HINT:** Combining the simplified ϵ and τ_{yy} equations yields a cubic equation for κ. It can be solved in closed form by assuming $\kappa = 0.4(1 + \delta)$, linearizing and solving for δ.

6.10 Consider the Wilcox multiscale model, Equations (6.66) - (6.72).

(a) State the limiting form of the equations for the incompressible, two-dimensional log layer.

(b) Assuming a solution of the form

$$\frac{dU}{dy} \sim \frac{u_\tau}{\kappa y}, \qquad k \sim \frac{u_\tau^2}{\sqrt{\beta^*}}, \qquad \omega \sim \frac{u_\tau}{\sqrt{\beta^*}\,\kappa y}$$

determine κ, $-\overline{u'v'}/k$, $\overline{u'^2}/k$, $\overline{v'^2}/k$, $\overline{w'^2}/k$ and e/k as algebraic functions of the closure coefficients. **HINT:** All are constant.

(c) Using the closure coefficient values in Equation (6.72), verify that $\kappa \approx 0.41$, $-\overline{u'v'}/k \approx 0.30$, $\overline{u'^2} : \overline{v'^2} : \overline{w'^2} \approx 4 : 2 : 2.6$, and $e/k \approx 0.75$.

6.11 Suppose we have flow in a coordinate frame rotating with angular velocity $\mathbf{\Omega} = \Omega\mathbf{k}$, where $\mathbf{k}$ is a unit vector in the z direction. The incompressible Navier-Stokes equation is

$$\rho\frac{d\mathbf{u}}{dt} + 2\rho\mathbf{\Omega} \times \mathbf{u} = -\nabla p - \rho\mathbf{\Omega} \times \mathbf{\Omega} \times \mathbf{x} + \mu\nabla^2\mathbf{u}$$

where $\mathbf{x}$ is position vector and d/dt is the Eulerian derivative. Verify that the Reynolds-stress equation's inertial terms in a two-dimensional flow are as follows:

$$\frac{d}{dt}\begin{bmatrix} \tau_{xx} & \tau_{xy} & 0 \\ \tau_{xy} & \tau_{yy} & 0 \\ 0 & 0 & \tau_{zz} \end{bmatrix} + \begin{bmatrix} -4\Omega\tau_{xy} & 2\Omega(\tau_{xx} - \tau_{yy}) & 0 \\ 2\Omega(\tau_{xx} - \tau_{yy}) & 4\Omega\tau_{xy} & 0 \\ 0 & 0 & 0 \end{bmatrix} = \cdots$$